

# Tale of Three Molecular Nitrides: Mononuclear Vanadium (V) and (IV) Nitrides As Well As a Mixed-Valence Trivanadium Nitride Having a V<sub>3</sub>N<sub>4</sub> Double-Diamond Core

Mehrafshan G. Jafari, Dominik Fehn, Anders Reinholdt, Cristina Hernández-Prieto, Prajay Patel, Michael R. Gau, Patrick J. Carroll, J. Krzystek, Cong Liu, Andrew Ozarowski, Joshua Telser,\* Massimiliano Delferro,\* Karsten Meyer,\* and Daniel J. Mindiola\*



Cite This: *J. Am. Chem. Soc.* 2022, 144, 10201–10219



Read Online

ACCESS |



Metrics & More

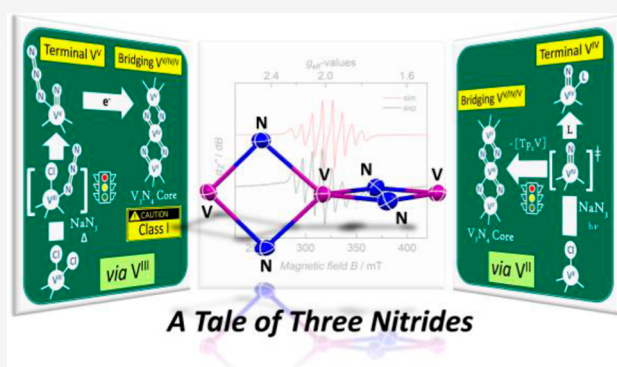


Article Recommendations



Supporting Information

**ABSTRACT:** Transmetalation of [VCl<sub>3</sub>(THF)<sub>3</sub>] and [TlTp<sup>tBu,Me</sup>] afforded [(Tp<sup>tBu,Me</sup>)VCl<sub>2</sub>] (**1**, Tp<sup>tBu,Me</sup> = hydro-tris(3-*tert*-butyl-5-methylpyrazol-1-yl)borate), which was reduced with KC<sub>8</sub> to form a C<sub>3v</sub> symmetric V<sup>II</sup> complex, [(Tp<sup>tBu,Me</sup>)VCl] (**2**). Complex **1** has a high-spin (*S* = 1) ground state and displays rhombic high-frequency and -field electron paramagnetic resonance (HFEP) spectra, while complex **2** has an *S* = 3/2 <sup>4</sup>A<sub>2</sub> ground state observable by conventional EPR spectroscopy. Complex **1** reacts with NaN<sub>3</sub> to form the V<sup>V</sup> nitride-azide complex [(Tp<sup>tBu,Me</sup>)V≡N(N<sub>3</sub>)] (**3**). A likely V<sup>III</sup> azide intermediate *en route* to **3**, [(Tp<sup>tBu,Me</sup>)VCl(N<sub>3</sub>)] (**4**), was isolated by reacting **1** with N<sub>3</sub>SiMe<sub>3</sub>. Complex **4** is thermally stable but reacts with NaN<sub>3</sub> to form **3**, implying a bis-azide intermediate, [(Tp<sup>tBu,Me</sup>)V(N<sub>3</sub>)<sub>2</sub>] (**A**), leading to **3**. Reduction of **3** with KC<sub>8</sub> furnishes a trinuclear and mixed-valent nitride, [(Tp<sup>tBu,Me</sup>)V<sub>2</sub>(μ<sub>4</sub>-VN<sub>4</sub>)] (**5**), conforming to a Robin–Day class I description. Complex **5** features a central vanadium ion supported only by bridging nitride ligands. Contrary to **1**, complex **2** reacts with NaN<sub>3</sub> to produce an azide-bridged dimer, [(Tp<sup>tBu,Me</sup>)V<sub>2</sub>(1,3-μ<sub>2</sub>-N<sub>3</sub>)<sub>2</sub>] (**6**), with two antiferromagnetically coupled high-spin V<sup>II</sup> ions. Complex **5** could be independently produced along with [(κ<sub>2</sub>-Tp<sup>tBu,Me</sup>)<sub>2</sub>V] upon photolysis of **6** in arene solvents. The putative {V<sup>IV</sup>≡N} intermediate, [(Tp<sup>tBu,Me</sup>)V≡N] (**B**), was intercepted by photolyzing **6** in a coordinating solvent, such as tetrahydrofuran (THF), yielding [(Tp<sup>tBu,Me</sup>)V≡N(THF)] (**B-THF**). In arene solvents, **B-THF** expels THF to afford **5** and [(κ<sub>2</sub>-Tp<sup>tBu,Me</sup>)<sub>2</sub>V]. A more stable adduct (**B-OPPh<sub>3</sub>**) was prepared by reacting **B-THF** with OPPh<sub>3</sub>. These adducts of **B** are the first neutral and mononuclear V<sup>IV</sup> nitride complexes to be isolated.



A Tale of Three Nitrides

## INTRODUCTION

The nitride functional group can derive from N<sub>2</sub> reduction and splitting by low-valent metal coordination complexes.<sup>1</sup> In biochemistry, the existence of a nitrogenase enzyme with vanadium in the active-site cofactor (FeV-co) is further impetus for research into vanadium coordination chemistry with ligands related to or derived from dinitrogen.<sup>2</sup> In solid-state chemistry, vanadium nitride surfaces may promote catalytic reduction<sup>3</sup> or oxidation<sup>4</sup> reactions and even exhibit superconductivity<sup>5</sup> at low temperatures. This promising material composed of a base metal is also attractive as an electrochemical capacitor given its high electronic conductivity, thermal stability,<sup>6</sup> high density, and high specific capacitance.<sup>7</sup> Although mononuclear anionic and neutral V<sup>V</sup> nitride complexes are known (Figure 1),<sup>10,w,8</sup> very little, if any, is known about mononuclear V<sup>IV</sup> nitrides, given their propensity to bridge and form oligomeric structures.<sup>9</sup> This is rather surprising given how the close derivative, vanadyl

([V≡O]<sup>2+</sup>),<sup>10</sup> is ubiquitous in coordination chemistry, energy storage technologies (e.g., redox-flow batteries),<sup>11</sup> and biological systems.<sup>12</sup> Moreover, molecular vanadium nitride complexes offer the enticing possibility of serving as well-defined precursors for vanadium nitride films.<sup>13</sup> However, there is currently a lack of atomically precise systems that demarcate how the transformation from molecules to a bulk material might proceed. In particular, a system in which a vanadium center is surrounded by only nitride ligands (and *vice versa*), while preserving a discrete architecture, remains unknown.

Received: January 9, 2022

Published: June 2, 2022



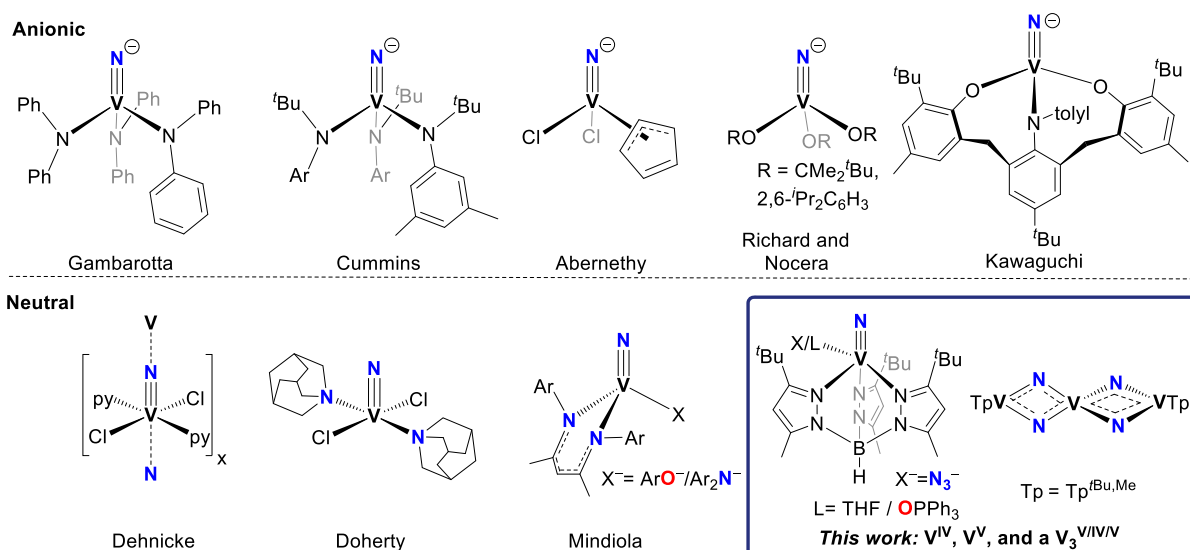
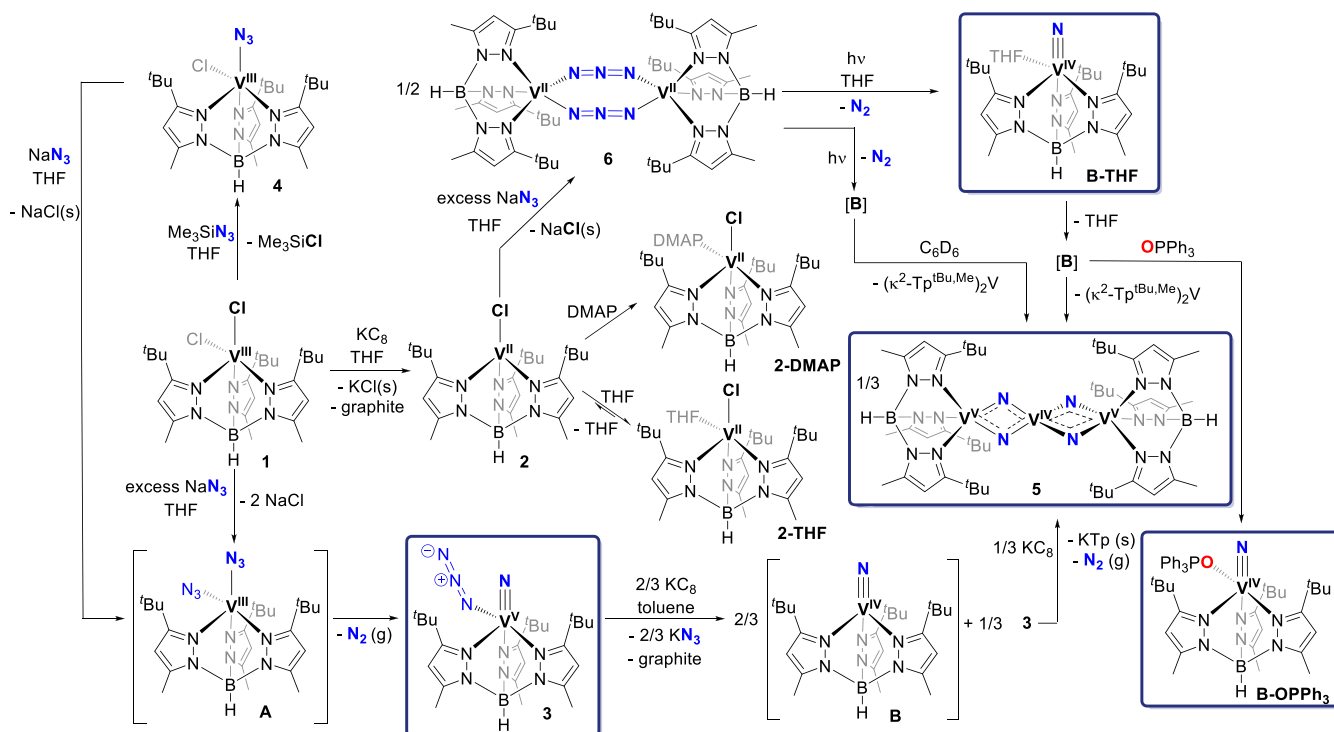


**Figure 1.** Examples of mononuclear vanadium nitrides. Counterions and solid-state aggregations are excluded for clarity. X and L represent a monoanionic and a neutral ligand, respectively. Specific details are provided in each case. Tp represents  $\text{Tp}^{\text{tBu,Me}}$ .

**Scheme 1. Synthesis of Chloride Precursors 1 and 2, along with THF/DMAP Adducts of 2, 2-THF, and 2-DMAP, Demonstrating Lewis Acidity of the  $\text{V}^{\text{II}}$  Center<sup>a</sup>**



<sup>a</sup>Metathesis of 1 with  $\text{NaN}_3$  and  $\text{Me}_3\text{SiN}_3$  produces azide and/or nitride species 3 and 4, respectively. Complex 3 likely forms *via* intermediates 4 and A as reaction of 4 with either  $\text{NaN}_3$  or excess  $\text{Me}_3\text{SiN}_3$  (at elevated temperatures) generates 3. Metathesis of 2 with  $\text{NaN}_3$  produces bis-azide complex 6. One-electron reduction of 3 produces trinuclear 5 *via* intermediate B; an alternative route commences with photolysis of 6 in arene solvents. Photolysis of 6 in THF stabilizes intermediate B by generating the adduct B-THF. B-THF gradually releases THF to form 5 and  $[(\kappa^2\text{-Tp}^{\text{tBu,Me}})_2\text{V}]$ . Reaction of B-THF with  $\text{OPPh}_3$  forms the more stable adduct B-OPPh<sub>3</sub>.

In this study (Scheme 1), we demonstrate synthetic entries to a rare, pseudo-tetrahedral, high-spin  $\text{V}^{\text{II}}$  complex,  $[(\text{Tp}^{\text{tBu,Me}})\text{VCl}]$  (2), which is readily prepared by one-electron reduction of the  $\text{V}^{\text{III}}$  precursor,  $[(\text{Tp}^{\text{tBu,Me}})\text{VCl}_2]$  (1,  $\text{Tp}^{\text{tBu,Me}}$  = hydro-tris(3-*tert*-butyl-5-methylpyrazol-1-yl)borate). We show how these  $\text{V}^{\text{II}}$  or  $\text{V}^{\text{III}}$  precursors can yield mononuclear  $\text{V}^{\text{IV}}$  and  $\text{V}^{\text{V}}$  nitrides as well as a unique trinuclear and mixed-valent

vanadium system with a central vanadium ion ligated only by bridging nitrides. We also show how a reactive mononuclear  $\text{V}^{\text{IV}}$  nitride can be generated by three independent routes and under the right conditions can be isolated and fully characterized. These nitride products, along with intercepted intermediates leading to the nitride functionality, have been isolated and structurally and spectroscopically characterized. The para-

magnetic vanadium systems have been studied by solution- and solid-state magnetometry. Conventional continuous wave (CW) X-band electron paramagnetic resonance (EPR) has been applied to half-integer (*i.e.*,  $V^{IV}$ ) species. In the case of complex **1**, which has an  $S = 1$  electronic ground state and, thus, is less suited for conventional EPR spectroscopy, we have applied high-frequency and -field EPR (HF-EPR) to better understand its electronic structure. Theoretical studies performed in parallel with experiments have also yielded a detailed picture of the bonding and electronic structure for this family of vanadium complexes and their respective nitrides.

## RESULTS AND DISCUSSION

**Tri- and Divalent Vanadium Complexes Supported by a Tripodal Monoanionic Ligand.** Recently, Petrov and co-workers reported the synthesis of a pseudo-tetrahedral divalent  $V^{II}$  complex,  $[(Tp^{tBu,tBu})VCl]$  ( $2^{tBu,tBu}$ ,  $Tp^{tBu,tBu}$  = hydro-tris(3,5-di(*tert*-butyl)pyrazol-1-yl)borate),<sup>14</sup> but did not explore its reactivity. Our own reaction studies revealed that the steric encumbrance imposed by the two  $tBu$  groups on the pyrazolyl moieties imparted too much strain on the B–N bonds for this chemistry to flourish. The degree of twisting of the sterically encumbered pyrazolyl groups in both **1**<sup>*tBu,tBu*</sup> and **2**<sup>*tBu,tBu*</sup> (Figure 2, left) may be taken as a portent of this system to decompose *via* ligand degradation. As a result, attempts to explore the chemistry

of  $2^{tBu,tBu}$  *via* transmetalation reactions with  $NaN_3$  led to undesired decomposition pathways, such as borotropic rearrangements that are common for early-transition metals bearing  $Tp$  ligand(s) (Scheme 2).<sup>15</sup> When excess  $NaN_3$  was

### Scheme 2. Reactivity Studies of Petrov's $[(Tp^{tBu,tBu})VCl]$ ( $2^{tBu,tBu}$ ) with Excess $NaN_3$ with or without Crown Ether

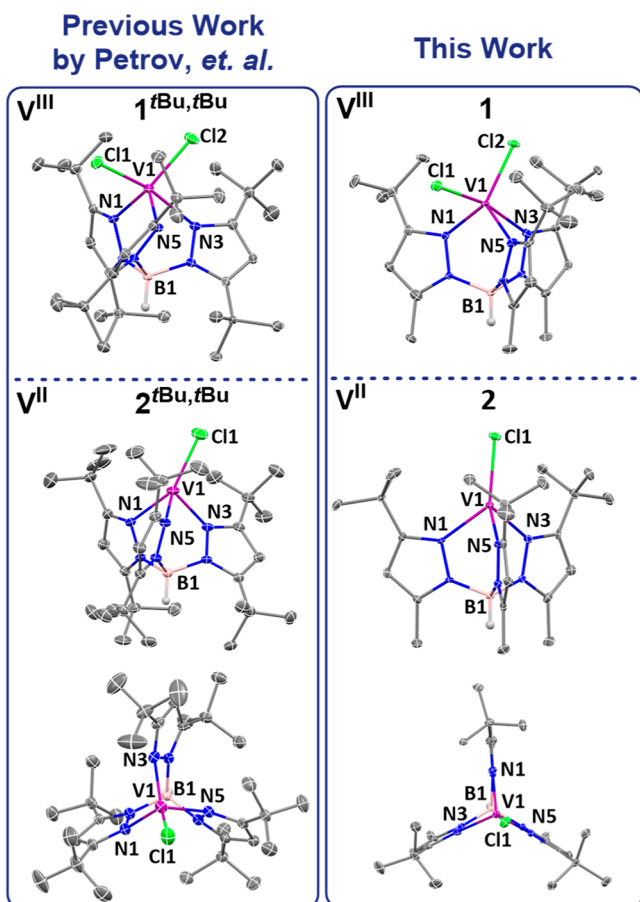
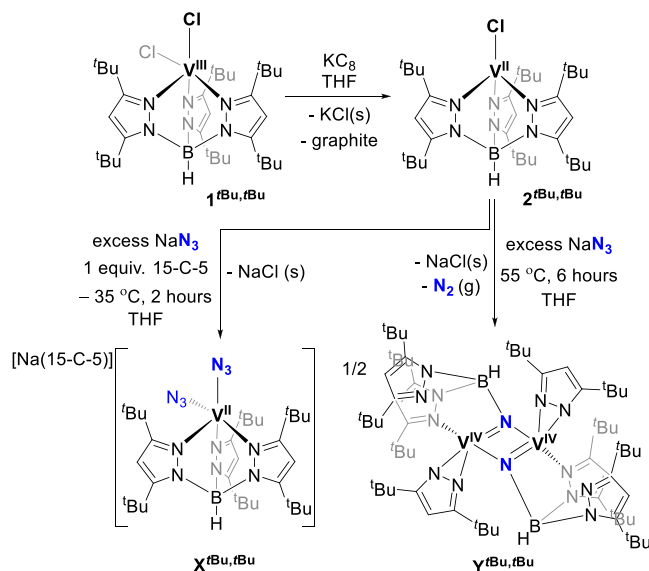


**Figure 2.** Structural representation of  $[(Tp^{tBu,tBu})VCl_2]$  (**1**<sup>*tBu,tBu*</sup>) and  $[(Tp^{tBu,tBu})VCl]$  (**2**<sup>*tBu,tBu*</sup>) (left) along with **1** and **2** (right; 50% thermal ellipsoid probability). Only one of the two molecules in the asymmetric unit (for **1** and **2**) is shown for simplicity. Disorder and hydrogen atoms (except B–H's) are excluded for clarity.

added to  $2^{tBu,tBu}$  in the presence of the crown ether, 15-C-5, the bis-azide ate complex  $[Na(15-C-5)][(Tp^{tBu,tBu})V(N_3)_2]$  ( $X^{tBu,tBu}$ ) was isolated in 92% yield (Scheme 2) and characterized by single-crystal X-ray diffraction (sc-XRD). On the other hand, performing the reaction in the absence of 15-C-5 under thermolytic conditions led to the dimeric ( $V^{IV}$ )<sub>2</sub> complex  $[\{hydro-bis(3,5-di(*tert*-butyl)pyrazol-1-yl)boraneimide\}V(3,5-di(*tert*-butyl)pyrazol-1-yl)]_2$  ( $Y^{tBu,tBu}$ ) in 47% yield, which was characterized by sc-XRD studies and multinuclear NMR spectroscopy. The latter complex is likely to form *via* the intermediacy of a reactive  $V^{IV}$  nitride,  $[(Tp^{tBu,tBu})V\equiv N]$ , which then undergoes ligand degradation and dimerization steps.

The molecular structure of  $X^{tBu,tBu}$  (Figure 3A) reveals the lack of threefold symmetry for the  $Tp^{tBu,tBu}$  ligand owing to significant skewing of the pyrazolyl arms to the same extent, if not greater, as in **1**<sup>*tBu,tBu*</sup>. The torsion angle,  $\angle V-N_{1,pz1}-N_{2,pz1}-B$ , for the most twisted pyrazolyl arm (pz1), defined as  $\xi_{twist}$ , provides a measure of the extent of skewing (a perfectly threefold symmetric  $Tp$  ligand would have  $\xi_{twist} = 0^\circ$ ; cf. Table S20 for the full list of  $\xi_{twist}$  angles of all pyrazolyl arms of all compounds discussed herein). In the case of  $X^{tBu,tBu}$ , the  $\xi_{twist}$  value is  $52.0(1)^\circ$ . In complex  $Y^{tBu,tBu}$  (Figure 3B), the average V–N and V=N bond distances are 1.986(3) Å and 1.735(3) Å, respectively, which are reminiscent of Cloke's  $[(L)V(\mu_2-N)_2V(L)]_2$  complex ( $L^{2-} = (Me_3Si)N\{CH_2CH_2N(SiMe_3)\}_2$ ), where the average V–N and V=N bond distances are 1.886 Å and 1.740 Å, respectively.<sup>9b</sup>

Based on the aforementioned results, we examined the less sterically encumbered, methyl-derivatized ligand,  $Tp^{tBu,Me}$ , reported originally by Trofimenko<sup>16</sup> and popularized by Theopold,<sup>17</sup> Parkin,<sup>18</sup> Takats,<sup>19</sup> and Anwander,<sup>20</sup> among others.<sup>21</sup> Accordingly, transmetalation of  $[VCl_3(THF)_3]$  with  $[TiTp^{tBu,Me}]_2$  in toluene at 65 °C afforded  $[(Tp^{tBu,Me})VCl_2]$  (**1**) in 75% yield as brick-orange plates after workup (Scheme 1). Single crystals of **1** could be obtained by  $Et_2O$ /toluene vapor

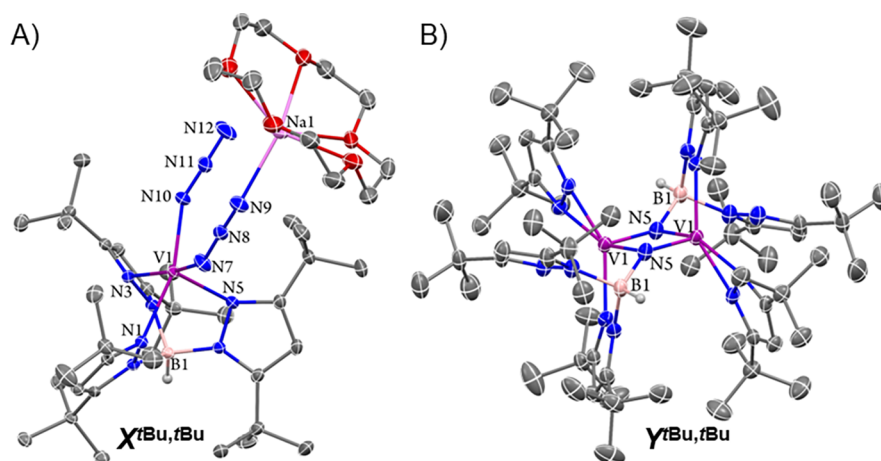


**Figure 3.** Structural representations (thermal ellipsoids at 50% probability) of (A)  $X^{tBu,tBu}$  and (B)  $Y^{tBu,tBu}$ . Hydrogen atoms (except B–H's), the second molecule in the asymmetric unit, and the co-crystallized solvent (in B) are excluded for clarity.

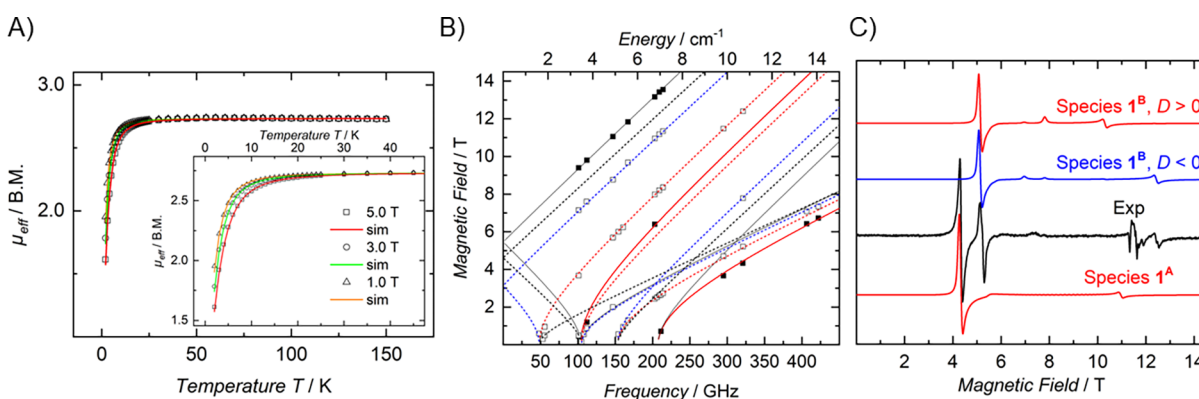


**Figure 4.** (A) VT-VF SQUID magnetization data of **1** with applied magnetic fields of 1, 3, and 5 T. (B) 2D plot of turning points in the powder spectra of **1** as a function of frequency (energy), marked as squares.  $1^A$ : full squares,  $1^B$ : empty squares. The curves ( $1^A$ : solid,  $1^B$ : dashed) were simulated using spin Hamiltonian parameters as in Table S1. Red curves: turning points with the magnetic field parallel to the  $x$ -axis of the zfs tensor; blue:  $B_0 \parallel z$ ; black:  $B_0 \parallel z$ . (C) HFEPR spectrum of **1** at 4.5 K and 321 GHz (black trace). The colored traces are simulations using spin Hamiltonian parameters of species  $1^B$  (top) and species  $1^A$  (bottom). For species  $1^B$ , simulations use positive  $D$  (red) and negative  $D$  (blue). For species  $1^A$ , the sign of  $D$  is undefined due to maximum rhombicity of the zero-field splitting (zfs) tensor. Simulation:  $1^A$ ,  $|D| = 5.4 \text{ cm}^{-1}$ ,  $E = 1.8 \text{ cm}^{-1}$ ,  $g_{\text{iso}} = 1.96$ ;  $1^B$ ,  $D = -4.3 \text{ cm}^{-1}$ ,  $|E| = 0.81 \text{ cm}^{-1}$ , and  $g_{\text{iso}} = 1.96$ ; the resonances at  $g = 1.96$  (11.7 T) most likely originate from a  $V^{IV}$  oxidation product.

diffusion at  $-35 \text{ }^\circ\text{C}$ . An sc-XRD study confirmed a five-coordinate  $V^{III}$  complex supported by a  $\kappa^3\text{-Tp}^{tBu,Me}$  chelate. With a  $\tau_5$  value<sup>23</sup> of 0.53 (Figure 2, top right), compound **1** falls midway between the limiting square pyramidal (SP) and trigonal bipyramidal (TBP) geometries,<sup>23</sup> whereas the chloride ligands are essentially orthogonal to each other ( $\text{Cl}-V-\text{Cl}_{\text{avg}}$ ,  $95.8(8)^\circ$ ). Complex **1** crystallizes with two crystallographically independent, but chemically equivalent, molecules in the asymmetric unit (space group  $Cc$ ), having  $B-V-Cl_{\text{anti}}$  angles of  $149.5(1)$  and  $150.2(3)^\circ$ . The  $V-Cl_{\text{avg}}$  bond distance of  $2.249 \text{ \AA}$  in  $1^{tBu,tBu}$  is similar to the  $V-Cl_{\text{avg}}$  bond distance of  $2.264 \text{ \AA}$  in **1**. Figure 2 shows a side-by-side comparison of  $1^{tBu,tBu}$  and **1**, which clearly reveals less twisting of the pyrazolyl arms in the methyl-substituted complex:  $\xi_{\text{twist}} = 62.0(5)^\circ$  in  $1^{tBu,tBu}$  and  $31.0(2)^\circ$  in **1**. This structural difference is even more pronounced for the four-coordinate  $V^{II}$  species (*vide infra*).

The UV–vis spectrum of **1** shows two absorption bands with maxima at 521 and 720 nm (d–d transitions:  $\epsilon = 229, 79 \text{ M}^{-1} \text{ cm}^{-1}$ ) with the first band showing a shoulder at 589 nm ( $\epsilon = 153 \text{ M}^{-1} \text{ cm}^{-1}$ ), cf. Supporting Information, Section S12.1, for more detailed discussion. The solution magnetic moment of complex **1** ( $\mu_{\text{eff}} = 2.71 \mu_B$ ; Evans' method, 300 K,  $C_6D_6$ ) corresponds to

the spin-only value for  $S = 1$ , appropriate for a  $d^2$  ion. Solid-state superconducting quantum interference device (SQUID) magnetization measurements of **1** (two independently prepared samples) were conducted in the temperature range of 2–150 K with applied magnetic fields of 1, 3, and 5 T (Figure 4A; only the first sample shown for clarity; cf. Supporting Information, Section S7.1). In agreement with solution data, both samples give  $\mu_{\text{eff}} = 2.72 \mu_B$  at 300 K, while below 10 K, the magnetic moment begins to decrease, ultimately reaching  $\mu_{\text{eff}} = 1.95 \mu_B$  at 2 K due to zero-field splitting (zfs). Fitting the magnetic data to a spin Hamiltonian for an  $S = 1$  species yielded the parameters  $D = 5.9 \text{ cm}^{-1}$ ,  $E/D = 0.33$ , and  $g_{\text{avg}} = 1.93$  (averaged fit values of the two independent batches).

Given the even number of unpaired electrons in **1**, we subjected a sample to HFEPR spectroscopy at 4.5 K. The frequency dependence of the HFEPR spectra (Figure 4B)<sup>24</sup> reveals two distinct species in the solid state, labeled  $1^A$  and  $1^B$ , with slightly different spin Hamiltonian parameters. This observation correlates with two crystallographically independent molecules of **1** in the crystal structure analysis (*vide supra*). Species  $1^A$  is characterized by a larger  $D$ -value of  $5.2 \text{ cm}^{-1}$  and the maximum rhombicity of the zfs tensor ( $E = 1.73 \text{ cm}^{-1}$ ),

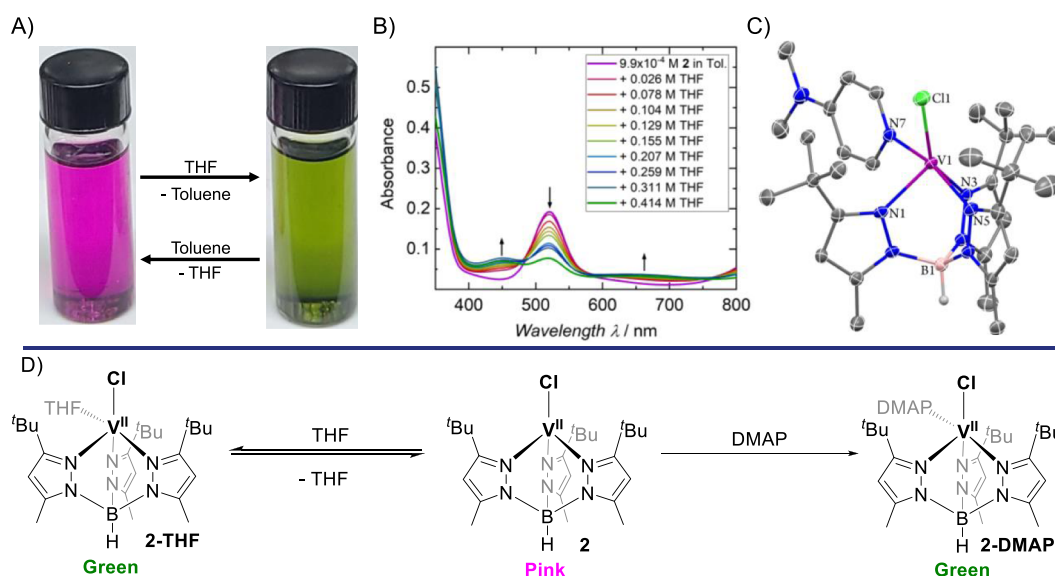


**Figure 5.** (A) Reversible color change of **2** when dissolved in non-coordinating (pink, e.g., in toluene) and coordinating solvents (green, e.g., in THF). (B) Titration (with THF) of **2** in toluene. (C) Structural representation of **2-DMAP** (thermal ellipsoids at 50% probability). Hydrogens (except B–H) are omitted for clarity. (D) Reversible coordination between **2** and THF (left) and the formation of **2-DMAP** (right).

while species **1<sup>B</sup>** has a smaller  $|D|$  value of  $4.3 \text{ cm}^{-1}$  and moderate rhombicity of the zfs tensor ( $|E| = 0.81 \text{ cm}^{-1}$ ). Simulations of single-frequency spectra, such as those shown in Figure 4C, proved that the sign of  $D$  for species **1<sup>B</sup>** is negative, while that of species **1<sup>A</sup>** is spectroscopically undefined because of the maximum rhombicity condition ( $|E/D| \approx 1/3$ ). However, since the magnitudes of the spectroscopic  $D$  values for **1<sup>A</sup>** and **1<sup>B</sup>** are similar to each other as well as to the  $D$  value determined for the bulk sample of **1** from SQUID magnetization, species **1<sup>A</sup>** and **1<sup>B</sup>** could conceivably have the same sign of  $D$ . The magnitude of  $D$  for **1** is less than that observed for six-coordinate, approximately octahedral  $\text{V}^{\text{III}}$  complexes ( $D \approx 7 \text{ cm}^{-1}$  for homoleptic complexes with O donors but larger for heteroleptic ones).<sup>25</sup> Four-coordinate, approximately tetrahedral  $d^2$  complexes (e.g.,  $\text{V}^{\text{III}}$ ,  $\text{Cr}^{\text{IV}}$ ) have very small (ideally zero) zfs.<sup>26</sup> We are not aware of zfs being determined for a five-coordinate  $\text{V}^{\text{III}}$  complex, so at present, the significance of the magnitude of zfs in **1** cannot be put into much context.<sup>a</sup> A possible structural origin for the difference in zfs parameters between **1<sup>A</sup>** and **1<sup>B</sup>** may be the slightly different metrics for the two molecules seen by sc-XRD (cf. Supporting Information, Section S12.1). This high sensitivity of HFEPR spectroscopy to structural changes is underlined by the failure of infrared (IR) ( $\nu_{\text{BH}} = 2563 \text{ cm}^{-1}$ , solid state) spectroscopy to distinguish crystallographic conformers of **1**. In solution (300 K,  $\text{C}_6\text{D}_6$ ),  $^1\text{H}$  NMR of complex **1** gives a single BH resonance and a single  $^1\text{H}$  NMR chemical environment for the pyrazolyl groups, suggesting rapid fluctuation of the molecule in solution (cf. Supporting Information, Section S4.3, Figure S14) and thus an ideally trigonal average structure.

Despite showing only non-reversible features, cyclic voltammetry (CV) studies of **1** (using  $0.1 \text{ M } [^n\text{Bu}_4\text{N}][\text{PF}_6]$  in THF) revealed both anodic and cathodic processes, thus suggesting chemical accessibility of oxidized and reduced derivatives of **1** (cf. Supporting Information, Section S10.1, Figure S106). Thus, chemical reduction of **1** with  $\text{KC}_8$  in THF generates a green solution, presumably containing five-coordinate  $[(\text{Tp}^{\text{tBu,Me}})\text{VCl}(\text{THF})]$  (**2-THF**). Upon removal of THF *in vacuo*, putative **2-THF** converts to four-coordinate  $[(\text{Tp}^{\text{tBu,Me}})\text{VCl}]$  (**2**),

isolated as pink crystals in 62% yield (Scheme 1, and Figure 5A). sc-XRD studies of **2** established a slightly distorted tetrahedral geometry ( $\tau_4 = 0.72$ )<sup>27</sup> around the  $\text{V}^{\text{II}}$  center with a tridentate grip of the  $\text{Tp}^{\text{tBu,Me}}$  ligand (Figure 2, bottom right). Akin to **1**, complex **2** has two crystallographically independent molecules in the asymmetric unit, with slightly different metrics. The average B–V–Cl angle of  $168.4(5)^\circ$  reveals some deviation of Cl from the B–V vector, presumably stemming from a Jahn–Teller effect, which is operative in a  $d^3$  ion in tetrahedral symmetry ( $^4\text{T}_1$  ground state;  $e^2t_2^1$ ). The B–V–Cl angle is closer to linearity in **2** than in Petrov’s  $2^{\text{tBu,tBu}}$  complex ( $157.7(9)^\circ$ ), most likely due to the lesser steric encumbrance of the Tp ligand. In  $2^{\text{tBu,tBu}}$  and **2**,  $\xi_{\text{twist}}$  equals  $46.6(1)$  and  $7.1(7)^\circ$ , respectively, revealing a distorted  $\text{Tp}^{\text{tBu,tBu}}$  ligand in  $2^{\text{tBu,tBu}}$  as opposed to a near-ideal threefold symmetric  $\text{Tp}^{\text{tBu,Me}}$  ligand in **2**. It is also notable that  $[(\text{Tp}^{\text{tBu,R}})\text{VCl}]$  ( $\text{R} = \text{tBu}$  or  $\text{Me}$ ) has roughly a  $\text{T}_d$  geometry when for a  $d^3$  system, ideal SP would be of lower energy than ideal  $\text{T}_d$  (cf. Supporting Information, Section S12.2). Indeed, a four-coordinate  $\text{V}^{\text{II}}$  complex with homoleptic monodentate ligands,  $[\text{V}(\text{OAr})_4\{\text{Li}(\text{THF})\}_2]$  ( $\text{Ar} = 2,6\text{-diisopropylphenyl}$ ), has an SP geometry.<sup>28</sup> Due to the larger ionic radius of  $\text{V}^{\text{II}}$  versus  $\text{V}^{\text{III}}$ , the average V–Cl bond distance in **2** exceeds that in **1** ( $\text{V–Cl}_{\text{avg}}$ :  $2.356(1) \text{ \AA}$  in **2** and  $2.264(3) \text{ \AA}$  in **1**). An  $\text{Et}_2\text{O}$  solution of **2** retains the pink color of the solid, indicative of a four-coordinate structure in solution. The vis–near IR (NIR) spectrum of **2** can be assigned and semi-quantitatively analyzed by ligand-field theory (LFT) as described in the Supporting Information (see Section S12.2). However, as discussed before, complex **2** readily binds THF to form **2-THF** (Scheme 1 and Figure 5D, left) as manifested by a reversible color change from pink ( $\text{Et}_2\text{O}$ ) to green (THF). When changing solvents from  $\text{Et}_2\text{O}$  to THF, the electronic absorption for **2** at  $520 \text{ nm}$  ( $\epsilon = 160 \text{ M}^{-1} \text{ cm}^{-1}$ ) undergoes a blue shift to  $457 \text{ nm}$  ( $\epsilon = 65 \text{ M}^{-1} \text{ cm}^{-1}$ ). In addition, the intense absorptions extending into the NIR region [ $893$  (infl),  $924$  (max), and  $960 \text{ nm}$  (infl)], with  $\epsilon = 130, 150$ , and  $130 \text{ M}^{-1} \text{ cm}^{-1}$ , respectively are replaced by weaker and broader features at  $668$  and  $855 \text{ nm}$  ( $\epsilon = 32, 19 \text{ M}^{-1} \text{ cm}^{-1}$ ). Along these lines, titration of a toluene solution of **2** with THF (0– $0.414 \text{ M}$ ) reveals three

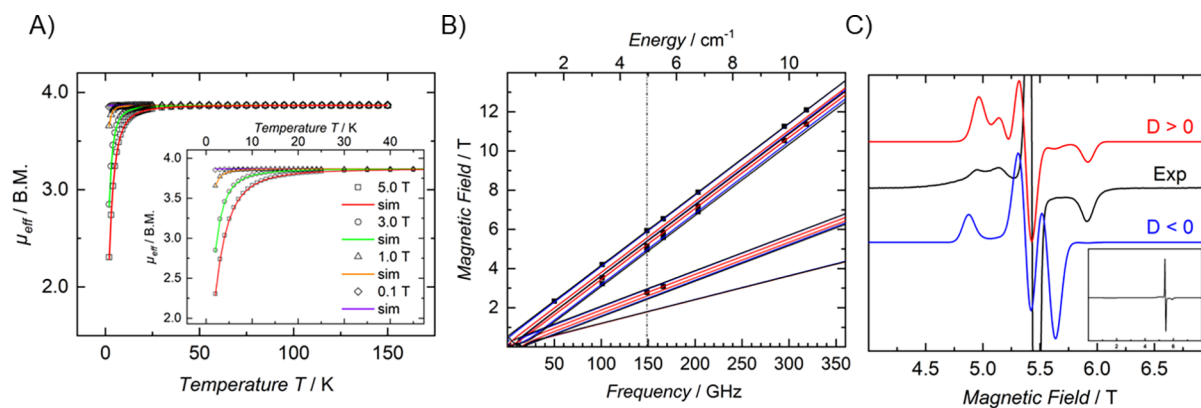


**Figure 6.** (A) VT-VF SQUID magnetization data of **2** at 5.0, 3.0, 1.0, and 0.1 T; experimental data are shown as squares, circles, triangles, and diamonds, respectively, and simulations are shown as red, blue, green, and purple traces, respectively. Simulation:  $S = 1.5$ ,  $D = 0.01 \text{ cm}^{-1}$ ,  $E/D = 0.33$ ,  $g_{\text{avg}} = 2.00$ . (B) 2D plot of turning points in the powder spectra of **2** as a function of frequency (energy), marked as squares. The curves were simulated using spin Hamiltonian parameters:  $S = 3/2$ ,  $|D| = 0.25(1) \text{ cm}^{-1}$ ,  $|E| = 0.058(5) \text{ cm}^{-1}$ , and  $g = [2.000(3), 1.96(1), 1.967(5)]$ . Red curves: turning points with the magnetic field parallel to the  $x$ -axis of the zfs tensor; blue:  $B_0 \parallel y$ ; black:  $B_0 \parallel z$ . The vertical dashed line represents the frequency (149 GHz) at which the spectrum in (C) was recorded. (C) Main plot: EPR spectrum of **2** at 4.5 K and 149 GHz (black trace). Colored traces are simulations using spin Hamiltonian parameters, where  $D$  is positive (red) or negative (blue):  $S = 3/2$ ,  $|D| = 0.24 \text{ cm}^{-1}$ ,  $|E| = 0.026 \text{ cm}^{-1}$ ,  $g = [1.97, 2.00, 1.97]$ . The experimental spectrum is dominated by a high-amplitude signal at  $g = 1.96$  from an  $S = 1/2$  impurity ( $V^{\text{IV}}$ , not simulated). *Inset*: the full experimental spectrum in the same conditions, indicating the absence of any  $V^{\text{III}}$  species.

clear isosbestic points and an association constant ( $K$ ) between **2** and THF on the order of  $1.2\text{--}3.6 \text{ M}^{-1}$  (Figure S5B, cf. Supporting Information, Section S8.4.1). Thus, in neat THF (12.3 M), **2** exists mainly as the five-coordinate adduct **2-THF** (94–98%). Notably, **2** displays a lower affinity toward THF than isostructural  $[(\text{Tp}^{\text{tBu,Me}})\text{TiCl}]$  ( $K_{\text{ass}} = 5\text{--}8 \text{ M}^{-1}$ ), highlighting the stronger Lewis acidity of a  $\text{Ti}^{\text{II}}$  versus  $\text{V}^{\text{II}}$  ion.<sup>29</sup> Similarly, cyclic voltammetry (CV) data for **2** dissolved in 1,2-difluorobenzene or THF (cf. Supporting Information, Section S10.2, Figure S107) show only a slight variation in oxidation and reduction potentials, possibly due to the reversible formation of **2-THF** in the latter case. In the cathodic scans, the reduction potentials for **2** in THF are anodically shifted by +0.02 V compared to **2** in 1,2-difluorobenzene, which readily converts to an equilibrium constant for the association of **2** with THF of  $2.2 \text{ M}^{-1}$ , in good agreement with UV–vis titrations. Despite multiple attempts at crystallization, we were unable to isolate **2-THF**, presumably due to the low association constant and/or volatility of the Lewis base. We therefore examined a stronger Lewis base such as DMAP. Accordingly, treatment of **2** with DMAP quantitatively produces green crystals of  $[(\text{Tp}^{\text{tBu,Me}})\text{VCl}(\text{DMAP})]$  (**2-DMAP**; Scheme 1 and Figure 5C). The solution magnetic moment of adduct **2-DMAP** ( $\mu_{\text{eff}} = 3.67 \mu_{\text{B}}$ ; Evans' method, 300 K,  $\text{C}_6\text{D}_6$ ) is consistent with a high-spin  $d^3$  system ( $S = 3/2$ ,  $g = 1.90$ ). The UV–vis spectra of **2-DMAP** and **2-THF** are qualitatively similar, whereas both differ markedly from the UV–vis spectrum of **2** (cf. Supporting Information, Sections S8.4 and 8.5, Figures S82 and S84). Most notably, the near-IR absorption band of **2** (924 nm) is absent for **2-DMAP** and **2-THF**, while the absorption band at 520 nm in **2** falls at a higher energy (394 nm) in **2-DMAP**.

Given the paramagnetic nature of **2**, magnetization studies were conducted. In solution, the magnetic moment of **2** indicates a mononuclear  $\text{V}^{\text{II}}$  ion with  $S = 3/2$  ( $\mu_{\text{eff}} = 3.78 \mu_{\text{B}}$ ; Evans' method, 300 K,  $\text{C}_6\text{D}_6$ ). Similarly, SQUID magnetometry for two independently prepared samples (2–300, 2–150 K shown in Figure 6A) showed the magnetic moment to be relatively constant between 10 and 300 K ( $3.87$  and  $3.84 \mu_{\text{B}}$  at 300 K), in accord with solution state data. However, below 10 K

and in an applied field of 1.0 T, the magnetic moment starts decreasing and reaches  $\mu_{\text{eff}} = 3.65\text{--}3.61 \mu_{\text{B}}$  at 2 K due to zfs (cf. Supporting Information, Section S7.2, Figures S66 and S67). At higher fields, the decrease becomes steeper, for example, leading to a magnetic moment of  $2.31 \mu_{\text{B}}$  at 2 K and 5.0 T (Figure 6A). Simulation of the magnetization data for **2** with an  $S = 3/2$  spin Hamiltonian yields  $D = +0.01 \text{ cm}^{-1}$ . Petrov's  $\mathbf{2}^{\text{tBu,tBu}}$  complex has a magnetic moment of  $3.78 \mu_{\text{B}}$  at 300 K and  $3.52 \mu_{\text{B}}$  at 2 K, thereby displaying essentially the same magnetic behavior as **2**.<sup>14</sup> As a spectroscopic complement to the magnetometric data, X- and Q-band EPR spectral data of **2** in glassy toluene (12 K) indicate a rhombic  $S = 3/2$  system with  $g_{\text{avg}} = 1.97$  (cf. Supporting Information, Section S5.1, Figure S43). Based on simulation of the X-band data,  $D$  and  $E$  are  $0.33$  and  $0.03 \text{ cm}^{-1}$ , respectively. On the other hand, Q-band spectra yield slightly different  $D$  and  $E$  ( $0.28$  and  $0.075 \text{ cm}^{-1}$ , respectively). The variation between X- and Q-band data reflects the challenging nature of deconvoluting numerous anisotropic linewidths simultaneous with features that potentially arise from various  $m_s$  transitions. To resolve this ambiguity, we studied a powdered sample of **2** by HF-EPR spectroscopy at 4.5 K, obtaining the frequency dependence of the resonances (Figure 6B,C; more details in the Supporting Information, Section S6.2). Here, the inter-Kramers transitions converge to a small energy of  $\sim 0.56 \text{ cm}^{-1}$ , which equals  $2D^*$  for  $S = 3/2$  ( $D^* = (D^2 + 3E^2)^{1/2}$ ). The complete set of frequency-independent spin Hamiltonian parameters is  $D = +0.25(1) \text{ cm}^{-1}$ ,  $E = 0.058(5) \text{ cm}^{-1}$ , and  $g = [2.000(3), 1.96(1), 1.967(5)]$ . The single-frequency spectra could be simulated using this set of parameters and prove that the sign of  $D$  is positive, and with the magnitude consistent with the values from frozen solution X- and Q-band EPR studies. This zfs is consistent with a simple LFT analysis (cf. Supporting Information, Section S12.2).

The frontier molecular orbitals of **2** (Figure 7) reveal an idealized  $C_{3v}$  symmetric system, where the energetic ordering for the vanadium 3d orbitals,  $d_{x^2-y^2} \approx d_{xy} < d_z^2 < d_{xz} \approx d_{yz}$ , essentially can be rationalized as the result of the chloride ligand being a stronger  $\sigma$ - and  $\pi$ -donor ligand than the weak-field  $[\text{Tp}^{\text{tBu,Me}}]$  ligand. This might hint that the  $[\text{Tp}^{\text{tBu,Me}}]$  ligand is bound

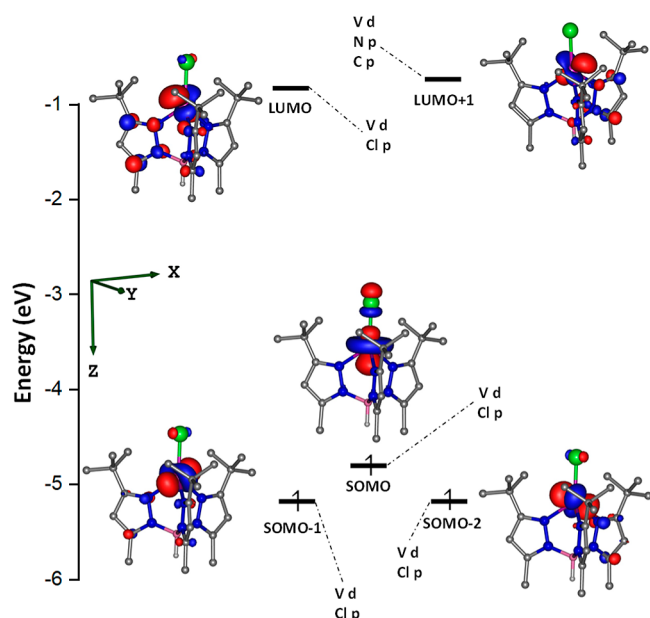


**Figure 7.** Calculated MO diagram for **2**. Orbital energies are in eV (B3LYP/TZVP).

relatively weakly to the vanadium center, and indeed, the tendency for the  $[\text{Tp}^{\text{tBu,Me}}]$  ligand to dissociate has a remarkable impact on the reactivity of its derivatives (*vide infra*). In the case of 2-DMAP (*cf.* Supporting Information, Section S11, Figure S117), coordination of a Lewis base breaks the threefold symmetry, and consequently, the degeneracy of the singly-occupied molecular orbital (SOMO) – 2 and SOMO – 1 orbitals computationally observed in **2** is broken.

**High-Valent Vanadium Nitrides and Intermediates Stemming from Complex 1.** At room temperature, complex **1** slowly reacts (overnight) with 2 equiv of  $\text{NaN}_3$  in THF to afford the azide-nitride complex  $[(\text{Tp}^{\text{tBu,Me}})\text{V}\equiv\text{N}(\text{N}_3)]$  (**3**) in 61% yield. After filtration of insoluble sodium salts, the reaction mixture must then be heated at 50 °C for an additional hour to ensure full conversion to **3** prior to workup (Scheme 1 and Figure 8B). Monitoring the reaction mixture by  $^1\text{H}$  NMR shows a new paramagnetic species that forms but then decays to **3**. We propose this intermediate to be either the mono-azide complex  $[(\text{Tp}^{\text{tBu,Me}})\text{V}(\text{Cl})(\text{N}_3)]$  (**4**, *vide infra*) or the bis-azide complex  $[(\text{Tp}^{\text{tBu,Me}})\text{V}(\text{N}_3)_2]$  (**A**). *sc*-XRD of **3** confirmed the terminal nature of the nitride moiety ( $\text{V}\equiv\text{N}_7$ : 1.558(2) Å and 1.565(5) Å), non-linear coordination of the azide ligand ( $\text{V}-\text{N}_8-\text{N}_9$ : 126.1(1) and 137.5(6)°), and a geometry confined between SP and TBP ( $\tau_3$ : 0.59 and 0.54) for the two polymorphs (Figure 8A and Table 1). Preparing the four  $^{15}\text{N}$ -enriched isotopomers,  $[(\text{Tp}^{\text{tBu,Me}})\text{V}\equiv\text{N}(^{15}\text{N}=\text{N}=\text{N})]$ ,  $[(\text{Tp}^{\text{tBu,Me}})\text{V}\equiv\text{N}(\text{N}=\text{N}=\text{N}^{15})]$ ,  $[(\text{Tp}^{\text{tBu,Me}})\text{V}\equiv\text{N}(^{15}\text{N}=\text{N}=\text{N}^{15})]$ , and  $[(\text{Tp}^{\text{tBu,Me}})\text{V}\equiv\text{N}(\text{N}=\text{N}=\text{N}^{15})]$  (collectively denoted as **3**- $^{15}\text{N}$ ) from complex **1** and  $\text{Na}(^{15}\text{N}=\text{N}=\text{N})$  revealed a characteristic, highly deshielded  $^{15}\text{N}$  NMR nitride resonance at 1035.8 ppm along with the expected two azide resonances at 212.2 and 243.9 ppm, corresponding to  $^{15}\text{N}$ -enriched  $\alpha$ - and  $\gamma$ -azide positions. IR spectral data of **3** (in KBr plates) show the prototypical signature of the azide group at 2079 and 2063  $\text{cm}^{-1}$  (in-phase/out-of-phase asymmetric stretching vibrations),<sup>30</sup> which red-shift to 2039 and 2054  $\text{cm}^{-1}$  for isotopomer **3**- $^{15}\text{N}$ , respectively (*cf.* Supporting Information, Section S9.6, Figure S99). The  $^1\text{H}$ - $\{^{11}\text{B}\}$  NMR spectrum of **3** shows one broad BH resonance at

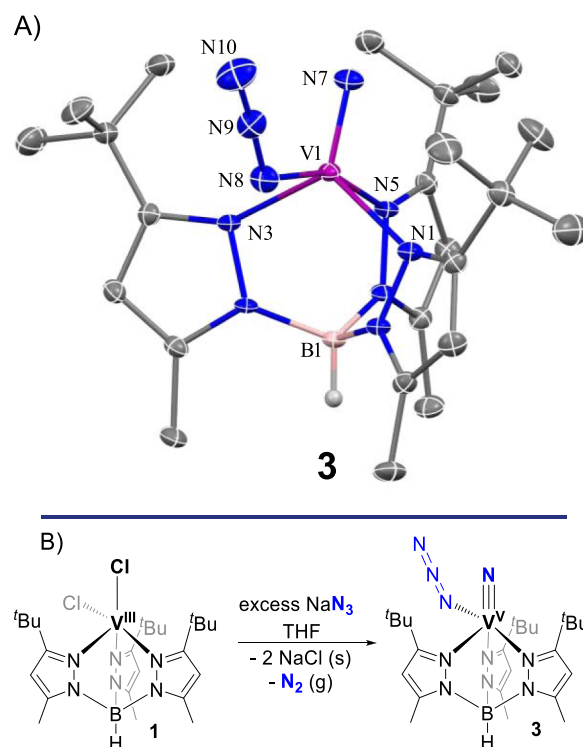


**Figure 8.** (A) Structural representation of nitride-azide complex **3** with thermal ellipsoids at 50% probability level. Hydrogen atoms (except the B–H) are omitted for clarity. (B) Synthesis of **3**.

**Table 1.** Salient Metric Parameters, NMR, and IR Spectroscopic Features of Vanadium Nitrides **3**, **5**, B-THF, and B-OPPh<sub>3</sub>

Complex	<b>3</b>	<b>5</b>	B-THF	B-OPPh <sub>3</sub>
$\text{VN}_{\text{nitride}}$ (Å)	1.558(2)	1.676(2) <sup>a</sup> 1.825(2) 1.872(2) 1.786(3)	1.578(2)	1.587(2)
$\tau_3$	0.59	0.76 <sup>b</sup>	0.52	0.48
$^{15}\text{N}$ NMR ( $\delta$ )	1035.8	n/a	n/a	n/a
$^{51}\text{V}$ NMR ( $\delta$ )	–246.3	n/a	n/a	n/a
$^{11}\text{B}$ NMR ( $\delta$ )	–35.9	–8.9	–19.3	–22.7
$\nu_{\text{BH}}$ ( $\text{cm}^{-1}$ )	2555	2550	2546	2558

<sup>a</sup>Only one half of the molecule is included for  $\text{VN}_{\text{nitride}}$  distances; *cf.* Figure 10B. <sup>b</sup> $\tau_4$  for the central  $\text{VN}_4$  fragment is measured as 0.79.

4.16 ppm along with three resonances from the  $\text{CH}_3$ ,  $\text{CH}$ , and  $^t\text{Bu}$  groups. This indicates the equivalence of the three pyrazolyl arms, consistent with rapid fluctuation of the molecule in solution at room temperature. As expected for a  $\text{V}^{\text{V}}$  complex, the UV–vis spectrum of **3** in pentane reveals no d–d transitions but only charge-transfer/ligand-centered bands at 388 (infl.), 310 (infl.), and 236 nm (max.) ( $\epsilon = 1660, 3060, \text{ and } 4940 \text{ M}^{-1} \text{ cm}^{-1}$ , respectively).

As mentioned previously, thermolysis is necessary to fully convert **1** and  $\text{NaN}_3$  into **3**. To our surprise, treatment of **1** with 1.05 equiv  $\text{Me}_3\text{SiN}_3$  produces the mono-azide complex  $[(\text{Tp}^{\text{tBu,Me}})\text{V}(\text{N}_3)\text{Cl}]$  (**4**) in 67% yield (Scheme 1 and Figure 9B), which was confirmed by a combination of structural (Figure 9A), spectroscopic ( $\nu_{\text{N}_3} = 1991 \text{ and } 2074 \text{ cm}^{-1}$ , *cf.* Supporting Information, Section S9.7, Figure S100), and

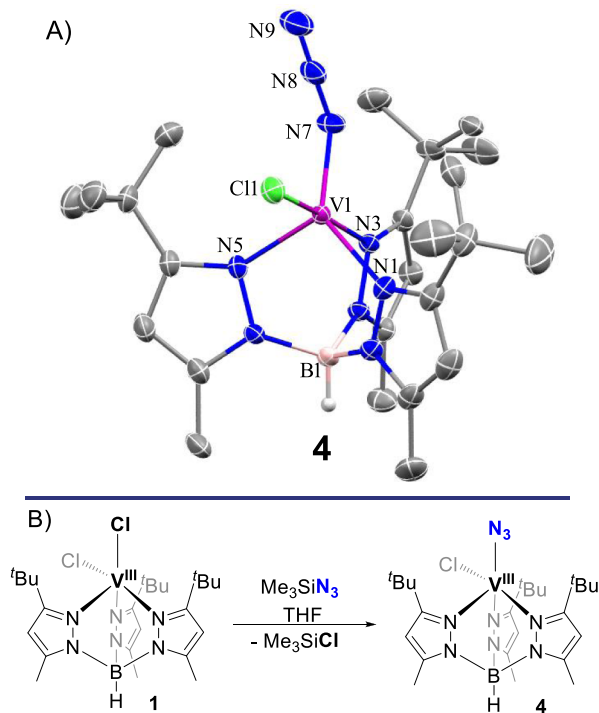


**Figure 9.** (A) Structural representation of complex **4** (thermal ellipsoids at 50% probability). Hydrogen atoms (except B–H) are omitted for clarity. (B) Synthesis of **4**.

magnetic studies ( $\mu_{\text{eff}} = 2.68 \mu_{\text{B}}$ ; Evans' method, 300 K,  $\text{C}_6\text{D}_6$ ;  $\mu_{\text{eff}} = 2.77 \mu_{\text{B}}$ ; SQUID, 300 K; corresponding to the spin-only moment for  $S = 1$  with  $g = 1.93(3)$ ). In terms of metrics, the V–Cl (2.327(9) Å) and V<sub>1</sub>–N<sub>7</sub> (1.896(3) Å) bonds in **4** are essentially orthogonal ( $\text{Cl}_1\text{–V}_1\text{–N}_7 = 94.0(4)^\circ$ ), and the  $\tau_5$  value of 0.69 suggests a geometry midway between SP and TBP. Although complex **4** shows all the features of a high-spin  $d^2$  ion, it is surprisingly stable to thermolysis (decomposition above 50 °C, cf. Supporting Information, Section S8.7, Figure S87) as well as photolysis. However, treatment of **1** with excess  $\text{Me}_3\text{SiN}_3$  (or treatment of **4** with  $\text{NaN}_3$ ), followed by heating to 45 °C overnight, leads to nitride-azide complex **3**. This points to **A** being a common intermediate in the conversion of **1** and **4** to nitride complex **3** (Scheme 1). It further suggests that the reaction of **1** with  $\text{NaN}_3$  traverses two transmetalation steps before  $\text{N}_2$  extrusion ensues. We have no definitive reason why complex **4**, as opposed to **A**, would be reluctant to undergo  $\text{N}_2$  elimination, but based on previous studies, we speculate that an azide ligand bridging across two V centers might play a critical role.<sup>8k,31</sup>

**Vanadium<sup>IV</sup> Nitrides from V<sup>V</sup> and V<sup>III</sup> Precursors.** As opposed to the ubiquitous vanadyl ion ( $[\text{VO}]^{2+}$ ), terminal V<sup>IV</sup> nitrides are exceedingly rare with the only crystallographically characterized example being dinuclear  $[\text{Na}]_2[(\text{nacnac})(\text{ArO})\text{–V}\equiv\text{N}]_2$  ( $\text{nacnac}^- = [\text{ArNC}(\text{CH}_3)_2\text{CH}^-$ ,  $\text{Ar} = 2,6\text{-}i\text{Pr}_2\text{C}_6\text{H}_3$ ), in which the vanadium centers are bridged by alkoxide and  $\text{Na}^+$ –arene interactions.<sup>8m</sup> In the above V<sup>IV</sup> example, other ligands than nitride are bridging, but there is however a tendency for nitride ligands themselves to bridge and form  $[\text{LM}(\mu_2\text{–N})_2\text{ML}]$  core structures, where M is a high-valent metal. Representative d-block examples involve V, Nb, Ta, Cr, and W.<sup>11,9b,32</sup> We therefore inquired if compound **3** could be reduced by one electron to yield a putative four-coordinate, neutral V<sup>IV</sup> nitride,  $[(\text{Tp}^{\text{tBu,Me}}\text{V}\equiv\text{N})]$  (**B**). In our case, treatment of **3** with  $\text{KC}_8$

furnishes an unprecedented trinuclear complex with four bridging nitride ligands,  $[(\text{Tp}^{\text{tBu,Me}}\text{V})_2(\mu_4\text{–VN}_4)]$  (**5**) in 54% isolated yield, where the central  $[\text{VN}_4]^{8-}$  unit could be considered analogous to the ubiquitous vanadate ion,  $[\text{VO}_4]^{3-}$  (Scheme 1 and Figure 10D, route 1). The connectivity of **5** was established by sc-XRD studies (Figure 10A,B), which reveal three vanadium centers arranged in a linear, double-diamond core fashion ( $\text{V}_1\text{–V}_3\text{–V}_2 = 177.45(3)^\circ$ ). The central vanadium (V<sub>3</sub>) is supported by only bridging nitride ligands, resulting in an approximately tetrahedral geometry, which is elongated along the V–V–V vector ( $\tau_4 = \tau_4' = 0.79$ , Table 1). This unique complex with a  $\text{V}_3\text{N}_4$  core (two diamond cores oriented orthogonally) has a similar tetrahedral geometry around the central vanadium, which has previously been computationally predicted for the metastable V<sup>IV</sup> nitride.<sup>33</sup> Within each  $\{\text{V}(\mu\text{–N})_2\text{V}\}$  fragment of **5**, the V–N bond distances are alternately short (1.676(3)–1.786(3) Å) and long (1.825(2)–1.884(3) Å, Figure 10B), which parallels Cloke's dinuclear  $[\{\text{N}(\text{N}''\text{V})_2(\mu\text{–N})_2\}]$  complex<sup>9b</sup> ( $(\text{N}(\text{N}''\text{V})_2)^{2-}$ :  $[(\text{Me}_3\text{Si})\text{N}(\text{CH}_2\text{CH}_2\text{N}(\text{SiMe}_3)_2)]_2^{2-}$ ), where the average V–N and V=N bond distances are 1.87 and 1.74 Å, respectively. The V<sub>distal</sub>–V<sub>central</sub> distances in **5** are 2.605(1) and 2.594(1) Å, which results in a separation of the two V<sub>distal</sub> of 5.198(1) Å. Notably, and given its composition, the formation of **5** requires expulsion of a  $\text{Tp}^{\text{tBu,Me}}$  ligand. When preparing **5** from **3** and  $\text{KC}_8$ , a lustrous black solid appears (graphite); we also observe  $\text{KN}_3$  (by IR spectroscopy) as well as  $[\text{KTp}^{\text{tBu,Me}}]$  (by <sup>1</sup>H NMR spectroscopy). Mass balance therefore suggests 2/3  $\text{KN}_3$  and 1/3  $[\text{KTp}^{\text{tBu,Me}}]$  (and 1/3  $\text{N}_2$ ) to form for each 1/3 equiv of **5**. From this complex reaction mixture,  $[\text{KTp}^{\text{tBu,Me}}]$  could be removed *via* fractional crystallization. Alternatively, addition of 1/3 equiv of  $[\text{VCl}_3(\text{THF})_3]$  generates **1**, and this could be readily separated from **5** due to the low solubility of **1** in alkanes (41% yield with respect to  $[\text{KTp}^{\text{tBu,Me}}]$ , Scheme 3). In a third approach,  $[\text{KTp}^{\text{tBu,Me}}]$  can be removed by extracting **5** into cold hexamethyldisiloxane and filtering the solution through Celite. This allows  $[\text{KTp}^{\text{tBu,Me}}]$  to be recovered, while isolating **5** in ~51% yield. Complex **5** can tantalizingly be thought of as an antiferromagnetically coupled adduct of an electron-deficient nitridyl “ $\text{VN}_2$ ” fragment and two units of putative **B**, overall leading to a doublet spin state. Therefore, **5** should be paramagnetic, and we indeed show how this species represents a trinuclear system with a mixed-valent  $\{\text{V}^{\text{V}}(\mu_4\text{–V}^{\text{IV}}\text{N}_4)\text{V}^{\text{V}}\}$  core. Solution magnetic measurements ( $\mu_{\text{eff}} = 1.89 \mu_{\text{B}}$ ; Evans' method, 300 K,  $\text{C}_6\text{D}_6$ ) corroborate this formulation, while X-band EPR (Figure 10C) shows the characteristic features of an  $S = 1/2$  species with hyperfine coupling to a single <sup>51</sup>V center ( $A = 91.4 \times 10^{-4} \text{ cm}^{-1}$ ,  $I = 7/2$ , 99.75%). Overall, the confinement of the unpaired electron to a single vanadium center is in line with a Robin–Day class I system.<sup>34</sup>

The calculated MO diagram of **5** suggests contribution of  $d_{x^2-y^2}$  orbitals on all three V centers in SOMO, but the unpaired electron is largely localized around the central V<sup>IV</sup> ion given that the SOMO is composed of orthogonal vanadium  $d_{x^2-y^2}$  orbitals which lack any constructive interactions (Figure 11). Notably, the SOMO is approximately 1.2 eV higher in energy than the other occupied orbitals as shown by restricted open (RO) B3LYP calculations, and the natural bond orbital analysis indicates that approximately 78% of the electron density in the SOMO is localized on the central vanadium atom, in accord with **5** having an eight-line EPR spectrum.

In pursuing the putative V<sup>IV</sup> nitride intermediate **B**, we turned to **2** and treated it with  $\text{NaN}_3$  in THF (in the dark) to form the

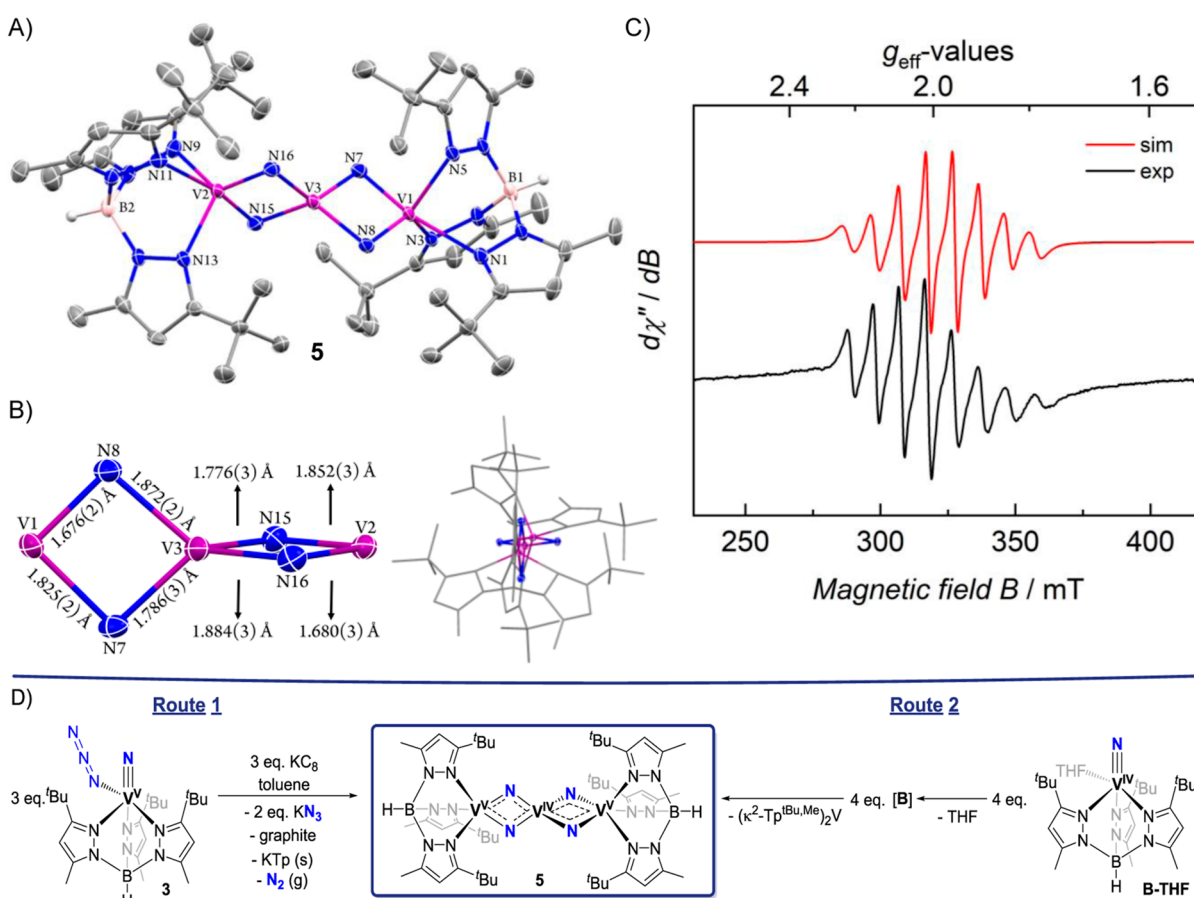
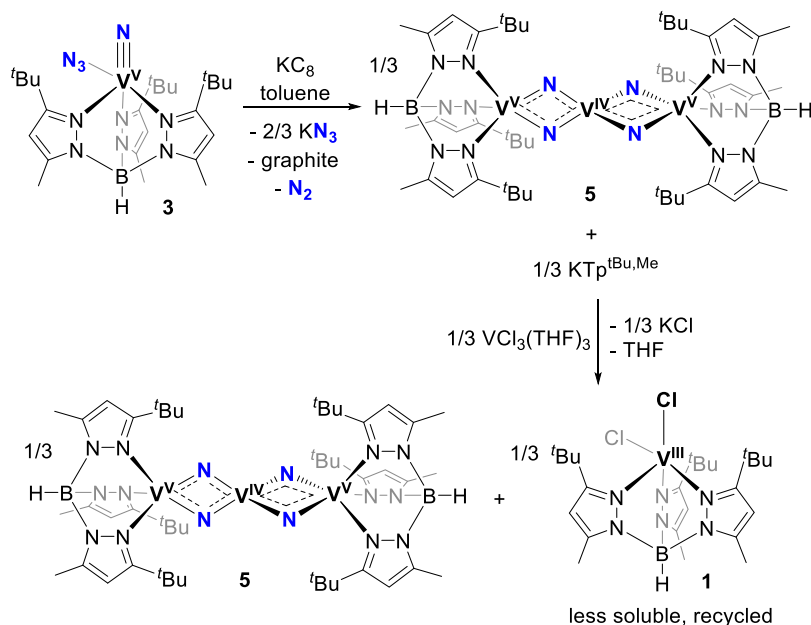


**Figure 10.** (A) Structural representation of complex **5** (thermal ellipsoids at 50% probability). Hydrogen atoms (except B–H's) and the co-crystallized solvent are omitted for clarity. (B) {V<sup>V</sup>(μ<sub>4</sub>-V<sup>IV</sup>N<sub>4</sub>)V<sup>V</sup>} core of **5** viewed from the side and along the V<sub>3</sub> axis. (C) CW X-band EPR spectrum of **5** in toluene at 293 K. Experiment (black trace). Simulation (red trace):  $g_{\text{iso}} = 1.98$ ,  $W_{\text{FWHM,iso}} = 2.03 \times 10^{-4} \text{ cm}^{-1}/\text{GHz}$ ,  $a_{\text{iso}} = 91.4 \times 10^{-4} \text{ cm}^{-1}$  ( $I = 7/2$  (<sup>51</sup>V), 99.75% nat. abundance). (D) Two independent syntheses of **5**.

**Scheme 3. Synthesis of Complex 5 from the Reduction of 3, Followed by Treatment with [VCl<sub>3</sub>(THF)<sub>3</sub>] to Form 1, Which Can Be Separated More Conveniently but Also Recycled**



azide-bridged dimer  $[(\text{Tp}^{\text{tBu,Me}}\text{V})_2(1,3\text{-}\mu_2\text{-N}_3)_2]$  (**6**) in 95% isolated yield (Scheme 1 and Figure 12D). The dimeric nature of

**6** was confirmed by sc-XRD (Figure 12A). As opposed to most mononuclear five-coordinate species presented above, complex

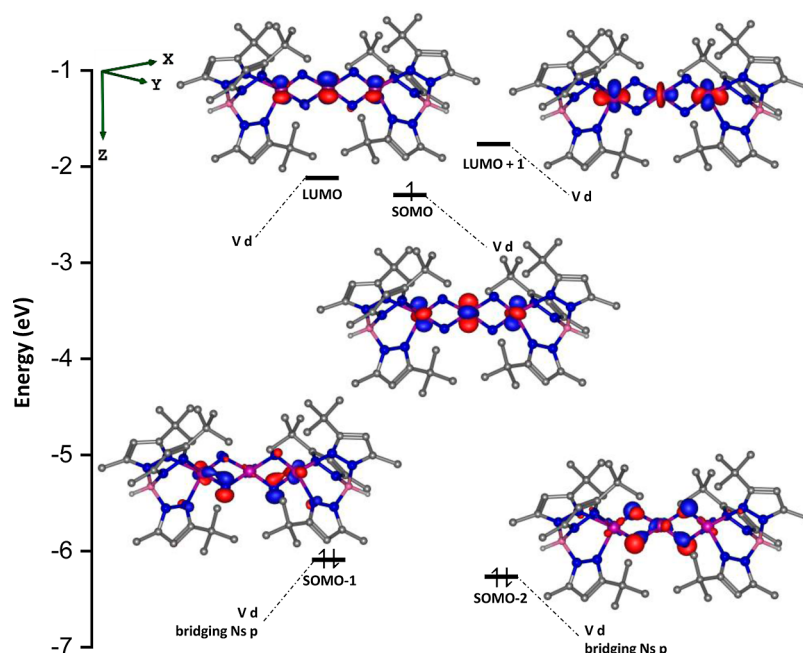


Figure 11. Calculated MO diagram of 5. Orbital energies in eV (RO-B3LYP/TZVP).

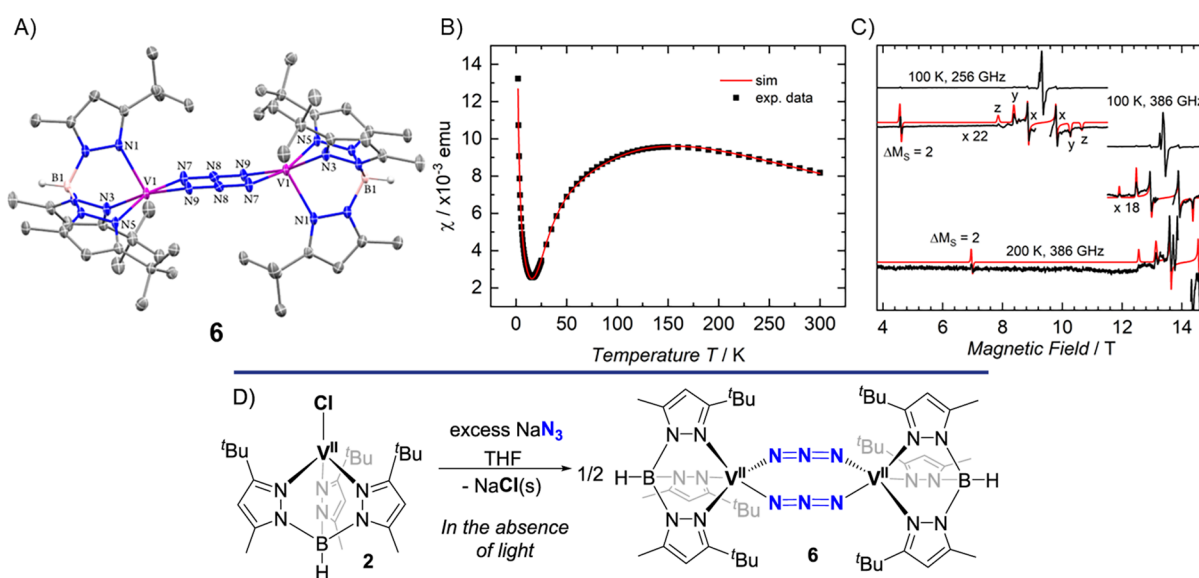


Figure 12. (A) Thermal ellipsoid plot of complex 6 (50% probability). Hydrogen atoms (except B–H) and co-crystallized toluene are omitted for clarity. (B) Magnetic susceptibility plot for a powder sample of 6 (at 1 T, black squares). Simulation (red trace):  $g_{ave} = 1.932$ ,  $J = -29.8 \text{ cm}^{-1}$ ,  $j = -1.80 \text{ cm}^{-1}$ ,  $TIP = 360 \times 10^{-6} \text{ cgs emu}$  (for each V), and paramagnetic impurity (i.e., monomeric  $V^{II}$ ) = 0.72%. (C) Black: HF-EPR spectra of 6 recorded at conditions indicated. Red: simulations of the (total spin)  $S = 1$  state spectra using  $g_x = 1.954$ ,  $g_y = 1.957$ ,  $g_z = 1.976$ ,  $D_{S=1} = -1.293 \text{ cm}^{-1}$ , and  $E_{S=1} = -0.145 \text{ cm}^{-1}$ . A strong central transition is cut off in the 386 GHz spectrum and in the magnified 256 and 368 GHz spectra. The “forbidden”  $\Delta m_s = 2$  transition is labeled. Labels  $x$ ,  $y$ , and  $z$  indicate the molecular orientations at which the respective transitions occur. (D) Synthesis of 6.

6 has a  $\tau_5$  value of 0.09, indicative of a nearly ideal SP geometry in which one of the pyrazolyl arms occupies the apical position. Notably, a similar SP geometry ( $\tau_5 = 0.06$ ) is observed in the bis-azide complex,  $[\text{Na}(15\text{-C-5})][(\text{Tp}^{t\text{Bu},t\text{Bu}})\text{V}(\text{N}_3)_2](\text{X}^{t\text{Bu},t\text{Bu}})$ .

Solid-state SQUID magnetization measurements (2–300 K) are consistent with a  $d^3$ – $d^3$  dimeric species with moderate antiferromagnetic coupling between the  $V^{II}$  centers (Figure 12B).  $\mu_{\text{eff}}$  of the dimeric species is  $4.42 \mu_B$  at 300 K, which corresponds to  $3.12 \mu_B$  per one V ion. At lower temperatures, the effective magnetic moment decreases steadily to reach  $0.45 \mu_B$  at 2 K. The effective magnetic moment determined by SQUID

magnetometry at 300 K is consistent with the value extracted by Evans’ method ( $\mu_{\text{eff}} = 4.48 \mu_B$  per dimer or  $3.16 \mu_B$  per V, 300 K,  $\text{C}_6\text{D}_6$ ) at the same temperature. Both values are lower than expected for an uncoupled spin-only ( $d^3$ )<sub>2</sub> system ( $\mu_{\text{eff}} = 3.87 \mu_B$  per one V), and notably, the consistency of the magnetic moments suggests 6 to remain dimeric in solution.

Antiferromagnetic exchange coupling of the form  $H = -2J\hat{S}_1\hat{S}_2$  in this system results in a diamagnetic ground state with a total spin of  $S = 0$ . States with  $S = 0, 1, 2$ , and 3 have energies of  $0, -2J, -6J$ , and  $-12J$ , respectively. All paramagnetic states are EPR-active, but only the  $S = 2$  state is observed in X-

band EPR as states  $S = 1$  and  $S = 3$  exhibit large zfs requiring higher field/frequencies. HF EPR spectra of **6** were recorded at 120–386 GHz. Spectral quality (Figure 12C) was sufficient to determine the spin Hamiltonian parameters of the  $S = 1$  state. The zfs parameters for  $S = 1$  of the dimer imply the zfs parameters of each  $V^{II}$  ion as  $D_V = +0.54 \text{ cm}^{-1}$  and  $E_V = +0.06 \text{ cm}^{-1}$ . The magnetic susceptibility data were then fitted using the “microscopic” spin Hamiltonian with  $D_V$  and  $E_V$  fixed as found from EPR (cf. Supporting Information, Section S6.3). It was found that the biquadratic exchange term,  $j(S_1S_2)^2$ ,<sup>35</sup> must be included to simulate the experimental magnetic data. This term appears very often in  $C_{II}^{III}$  dimers with the same  $d^3$ – $d^3$  configuration as our  $V^{II}$  dimer.<sup>36</sup>

We propose complex **6** to extrude  $N_2$  both thermolytically and photolytically, with photolysis giving the cleanest conversion. Accordingly, irradiation of **6** in toluene with a Xe or a 390 nm LED lamp over 2 h generated the trinuclear species **5**. The requisite release of  $Tp^{tBu,Me}$  was traced to a new paramagnetic species,  $[V(\kappa^2-Tp^{tBu,Me})_2]$ , identified on the basis of an sc-XRD study. Due to the similar solubilities of **5** and the divalent  $V^{II}$  complex, spectroscopically pure  $[V(\kappa^2-Tp^{tBu,Me})_2]$  could not be isolated (Scheme 1 and Figure 13). The  $Tp^{tBu,Me}$  ligands in

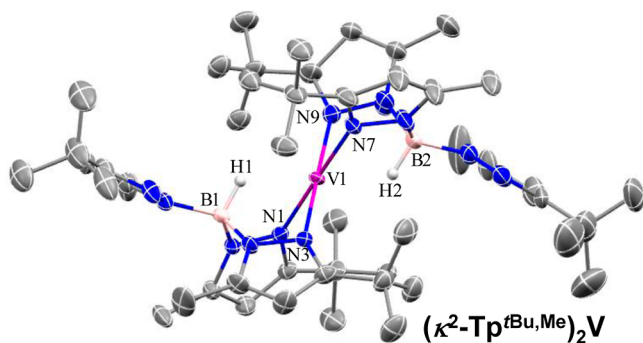


**Figure 13.** Structural representation of the complex  $[V(\kappa^2-Tp^{tBu,Me})_2]V$  (thermal ellipsoids at 50% probability). Hydrogen atoms (except B–H) and co-crystallized toluene and pentane are omitted for clarity.

$[V(\kappa^2-Tp^{tBu,Me})_2]$  seemingly bind in a bidentate fashion, which defines a square planar motif around vanadium ( $N-V-N = 85.5(7)$  and  $85.6(5)^\circ$ ,  $\tau_4 = 0.04$ ). However,  $[V(\kappa^2-Tp^{tBu,Me})_2]$  is more appropriately seen as an octahedral complex containing *transoid* BH donor groups ( $V-H = 1.984(1)$  and  $1.967(1) \text{ \AA}$ ). Returning to the formation of **5** from **6**, a  $V^{II}$  ion sequesters the excess equivalent of  $Tp^{tBu,Me}$ , which stands apart from the reduction of compound **3** to generate **5** and  $[KTp^{tBu,Me}]$ . We propose **6** to photolytically extrude  $N_2$  by forming **B**, which then undergoes a series of ligand-exchange reactions with three more equivalents of **B**. The Lewis acidity of **B** and the ability of the nitride and pyrazolyl groups to bridge between vanadium centers are most likely reasons why a unique complex such as **5** forms. Attempts at preparing  $[V(\kappa^2-Tp^{tBu,Me})_2]$  independently from **2** and 1 equiv  $[TITp^{tBu,Me}]$  or from  $[VCl_2(tmeda)]$  and 2 equiv  $[TITp^{tBu,Me}]$  were unsuccessful (cf. Supporting Information, Section S3.13), which lends support for a mechanism in which several units of **B** aggregate prior to releasing **5** and  $[V(\kappa^2-Tp^{tBu,Me})_2]$ .

**Trapping of the Mononuclear  $V^{IV}$  Nitride **B**.** Given the photochemical formation of **5** upon photolysis of **6** in toluene, we conducted the same experiment in a coordinating solvent. Irradiation of **6** in THF at 293 K over 30 min to several hours (Figure 14D) resulted in gradual decay of the X-band EPR

signals from the precursor concurrent with growth of a new signal consistent with a new radical distinct from **5** (Figure 14A). Gratifyingly, photolysis of **6** on a preparative scale quantitatively afforded the new paramagnetic species, which was identified as the Lewis base adduct of the elusive terminal  $V^{IV}$  nitride **B**, namely,  $[(Tp^{tBu,Me})V\equiv N(THF)]$  (**B-THF**), on the basis of an sc-XRD study (Scheme 1 and Figure 14B). The solid-state structure of **B-THF** exhibits some disorder of the  $tBu$  groups and THF ligands. As expected, based on the larger ionic radius of  $V^{IV}$  compared to  $V^V$ , the  $V\equiv N$  bond in **B-THF** ( $1.580(2) \text{ \AA}$ ) is slightly longer than in **3** ( $1.561(5) \text{ \AA}$ ). On the other hand, the  $V\equiv N$  bond distance is somewhat shorter in **B-THF** than in the only other reported  $V^{IV}$  nitride complex, namely, dinuclear  $[Na]_2[(nacnac)(ArO)V\equiv N]_2$  ( $V\equiv N: 1.624(2)$  and  $1.614(3) \text{ \AA}$ ). Like most other five-coordinate species in this work, **B-THF** falls midway between the limiting TBP and SP geometries ( $\tau_5 = 0.52$ , Table 1). Despite being stable for days at  $-35^\circ\text{C}$  in THF, the complex **B-THF** slowly decomposes at room temperature in the solid state (*vide infra*). The X-band EPR spectrum of **B-THF** (Figure 14C) shows the signature eight-line pattern from hyperfine coupling of the unpaired electron to the  $^{51}V$  center ( $a_{iso} = 123 \times 10^{-4} \text{ cm}^{-1}$ , 369 MHz). This  $^{51}V$  isotropic hyperfine coupling is  $\sim 15\%$  greater than that observed for vanadyl with five exclusively O-donor ancillary ligands ( $318$ – $328 \text{ MHz}$ )<sup>37</sup> and is much larger than in vanadyl porphyrins ( $263 \text{ MHz}$ ).<sup>38</sup> Clearly, **B-THF** is a vanadium-centered paramagnet. This character of complex **B-THF** was also established by solution magnetometry ( $\mu_{eff} = 1.95 \mu_B$ ; Evans' method, 300 K, THF- $d_6$ ), corresponding to  $S = 1/2$ . Last, preparing the 50%  $^{15}N$  enriched isotopomer  $[(Tp^{tBu,Me})V\equiv^{15}N(THF)]$  (**B-THF- $^{15}N$** ), *via* photolysis of **6- $^{15}N$** , did not alter the X-band EPR spectral features, further indicating the nitride group to have minimal nitridyl character. This is likely the result of the unpaired electron residing in a d-orbital with delta symmetry with respect to the  $V-N_{nitride}$  axis.<sup>39</sup> This result is consistent with Bendix' studies of isoelectronic  $Cr^V$  terminal nitride complexes with an SP or octahedral geometry; here, hyperfine coupling to the axial nitride  $^{14}N$  is obscured by unresolved coupling to equatorial ligands such as  $^{35,37}Cl$  ( $I = 3/2$ , 100%), whereas coupling to the nitride is resolved when the equatorial ligands are  $^{16}O$  (from the dibenzoylmethane ligand, dbm; modeled as acac for calculations).<sup>40</sup> In **B-THF- $^{15}N$** , unresolved hyperfine coupling to pyrazolyl  $^{14}N$  (three coordinated, three not) prevents resolution of the small coupling to nitride  $^{14,15}N$ .<sup>41</sup>

When dissolving the complex **B-THF** in  $C_6D_6$  for NMR spectroscopic characterization, the  $V^{IV}$  nitride rapidly transforms to **5** and  $[V(\kappa^2-Tp^{tBu,Me})_2]$  (Scheme 1, and Figure 10D). In general, **B-THF** is quite unstable in weakly coordinating solvents. Presumably, the lack of a Lewis base allows the unsaturated  $V^{IV}$  center in **B** to oligomerize *via* bridging nitride and/or pyrazolyl moieties. As a result, we propose that dissolution of **B-THF** in hydrocarbon solvents results in dissociation of THF that is accompanied with bimolecular reactions, eventually disproportionating to **5** and  $[V(\kappa^2-Tp^{tBu,Me})_2]$ . Surprisingly, there is no structurally characterized example of a neutral  $[V(Tp)_2]^0$  complexes that exist in the literature.<sup>42</sup> Based on the above studies, it is clear that **B** is highly reactive, probably because it has a d-electron count of only 13 valence electrons. Due to the instability of **B-THF**, we turned to a stronger Lewis base that could trap **B** without compromising the nitride ligand, namely,  $OPPh_3$ . Photolysis of **6** in THF in the presence of 2 equiv of  $OPPh_3$  generated the **B- $OPPh_3$**  adduct in

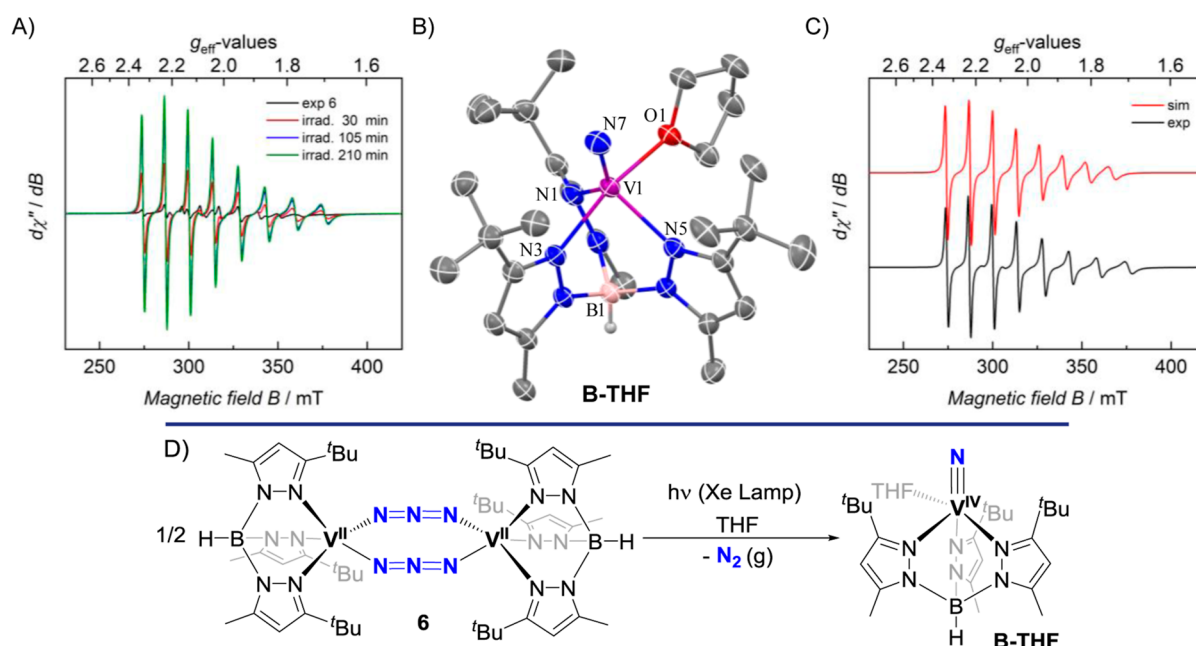


**Figure 14.** (A) CW X-band EPR spectra of pristine 6-<sup>14</sup>N in THF at 293 K (black trace) and after irradiation. (B) Structural representation of the complex B-THF (thermal ellipsoids at 35% probability). Hydrogen atoms (except B-H), the co-crystallized solvent, and disorder on THF and <sup>t</sup>Bu groups are omitted for clarity. (C) CW X-band EPR spectrum of B-THF in THF at 293 K (black trace). Simulation (red trace):  $S = 1/2$ ,  $g_{\text{iso}} = 1.99$ , and  $W_{\text{FWHM,iso}} = 2.00 \times 10^{-4} \text{ cm}^{-1}/\text{GHz}$ . Hyperfine coupling to one <sup>51</sup>V ( $I = 7/2$ , 99.75%)  $a_{\text{iso}} = 123 \times 10^{-4} \text{ cm}^{-1}$ . (D) Photolysis of 6 leading to B-THF.

near-quantitative yield (94%, Scheme 1 and Figure 16B). The complex B-OPPh<sub>3</sub> resembles B-THF structurally with a  $\tau_3$  value

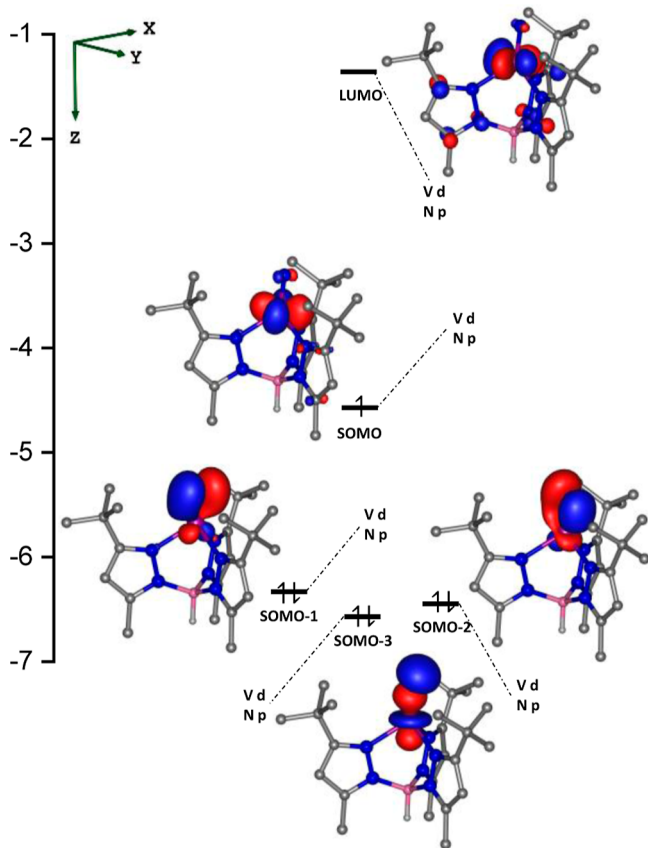


**Figure 15.** MO diagrams of B. Orbital energies reported in eV (B3LYP/TZVP).

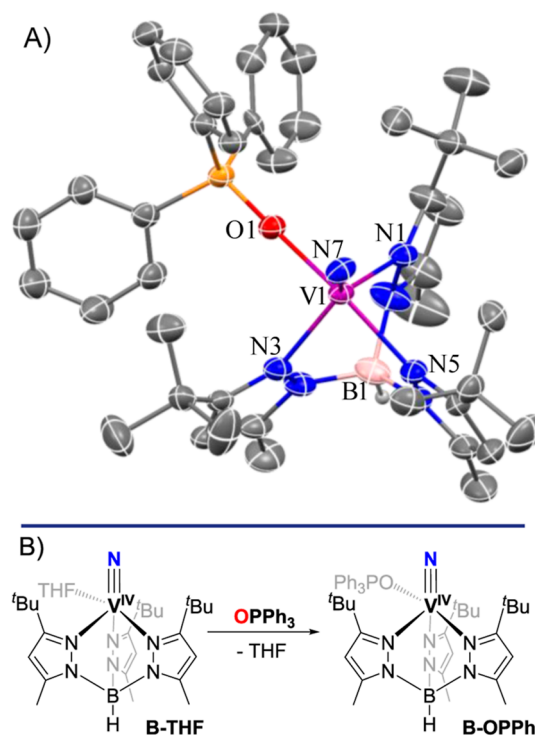


**Figure 16.** (A) Structural representation of the complex B-OPPh<sub>3</sub> (thermal ellipsoids at 50% probability). Hydrogen atoms (except B-H) are omitted for clarity. (B) Reaction between B-THF and OPPh<sub>3</sub> to furnish B-OPPh<sub>3</sub>.

of 0.48 (Table 1). The V≡N bond distance in B-OPPh<sub>3</sub> (1.587(2) Å) is slightly longer than that in B-THF (Figure 16A, Table 1), most likely the result of OPPh<sub>3</sub> being a stronger  $\sigma$ -donor ligand than THF. The cyclic voltammograms of B-THF and B-OPPh<sub>3</sub> reveal a reversible one-electron anodic event for

each complex. The reduction potentials are +0.38 and +0.08 eV for **B-THF** and **B-OPPh<sub>3</sub>**, respectively, suggesting oxidation of these species to a terminal V<sup>V</sup> nitride to be reversible as well as highly tunable through the choice of a Lewis base (cf. Supporting Information, Sections S10.4 and S10.5, Figures S110 and S113). The voltammogram of **B-OPPh<sub>3</sub>** further reveals a multi-electron cathodic process at a negative potential (−1.53 eV, Figure S112).

Figure 15 shows the calculated MO diagram of **B** (geometry optimized after removing L from the sc-XRD structure of **B-L**); MO diagrams of the adducts **B-OPPh<sub>3</sub>** and **B-THF** are presented in Figures S122 and S123, respectively. The most salient bonding features for **B** are a V≡N triple bond, composed of the SOMO − 3 (σ-symmetric combination of V 3d<sub>z<sup>2</sup></sub>/N 2p<sub>z</sub> atomic orbitals), SOMO − 2, and SOMO − 1 (orthogonal, π-symmetric combinations of V 3d<sub>yz</sub>/N 2p<sub>y</sub> and the V 3d<sub>xz</sub>/N 2p<sub>x</sub> atomic orbitals). The SOMO essentially consists of a V 3d<sub>xy</sub> orbital, which is δ-symmetric along the V≡N direction (z-axis) and, therefore, interacts insignificantly with 2s and 2p orbitals of the nitride ligand. This is in accordance with the minimal <sup>14,15</sup>N hyperfine coupling observed by EPR (vide supra, Figure 14C and Supporting Information, Section S5.4). In analogy to **B**, the adducts, **B-THF** and **B-OPPh<sub>3</sub>**, each displays a V≡N triple bond and has an unpaired electron in a d<sub>xy</sub> orbital. However, while the lowest unoccupied molecular orbital (LUMO) of **B** is largely confined to the metal center, the LUMOs of **B-OPPh<sub>3</sub>** and **B-THF** are instead ligand-based (cf. Supporting Information, Section S11, Figures S122 and S123).

## CONCLUSIONS

We have used a sterically demanding hydro-tris(pyrazolyl)-borate ligand, [Tp<sup>tBu,Me</sup>]<sup>−</sup>, to synthesize the spin triplet V<sup>III</sup> complex [(Tp<sup>tBu,Me</sup>)VCl<sub>2</sub>] (**1**). Replacement of the pyrazoles' 5-tBu groups with less bulky Me substituents resolved the propensity for the previously reported [(Tp<sup>tBu,tBu</sup>)VCl<sub>2</sub>] to undergo ligand degradation, while preserving a sterically encumbering environment. Reduction of **1** affords a high-spin (*S* = 3/2) and mononuclear V<sup>II</sup> complex, [(Tp<sup>tBu,Me</sup>)VCl] (**2**) with a <sup>4</sup>A<sub>2</sub> electronic ground-state, established by solution- and solid-state magnetometry as well as EPR and HFEPN spectroscopy. The affinity of **2** toward THF and 4-dimethylaminopyridine (DMAP) reveals its Lewis acidity and proclivity to attain five-coordination. Two-step transmetallation of **1** with NaN<sub>3</sub>, followed by N<sub>2</sub> extrusion, affords a diamagnetic V<sup>V</sup> nitride, **3**. Using Me<sub>3</sub>SiN<sub>3</sub> as an azide source, we isolated and characterized an unexpected intermediate, the V<sup>III</sup> azide-chloride complex, **4**, which converts to **3** upon exposure to additional azide. Attempts at reducing **3** to a V<sup>IV</sup> nitride affords the unprecedented trinuclear tetra-nitride **5**. Solution magnetometry and EPR studies of complex **5** reveal one unpaired electron confined to a single vanadium center, in accord with a Robin–Day class I system. In an alternative approach, we explored photolysis of the dinuclear V<sup>II</sup> azide **6**. In toluene, this affords **5** and [V(κ<sup>2</sup>-Tp<sup>tBu,Me</sup>)<sub>2</sub>], while in THF, this furnishes a neutral, mononuclear V<sup>IV</sup> nitride, **B-THF**, where **B** is the still elusive four-coordinate [(Tp<sup>tBu,Me</sup>)V(≡N)]. Use of a stronger Lewis base, such as OPPh<sub>3</sub>, led to the kinetically stable V<sup>IV</sup> nitride, **B-OPPh<sub>3</sub>**. Notably, the unpaired electron in the V<sup>IV</sup> nitride species is metal-centered as seen from the vanishing hyperfine coupling to the nitride ligand and the typical <sup>51</sup>V coupling. We thus report the first example (as **B-L**, **B** = (Tp<sup>tBu,Me</sup>)V(≡N), L = THF, or OPPh<sub>3</sub>) of a neutral mononuclear [V≡N]<sup>+</sup> (azavanadyl) analogue to the many such [V≡O]<sup>2+</sup> (vanadyl) species.

Overall, we have demonstrated how the [Tp<sup>tBu,Me</sup>]<sup>−</sup> ligand can accommodate low-valent vanadium centers but also support high-valent V<sup>V</sup> and V<sup>IV</sup> nitrides in mononuclear or trinuclear forms. The latter, compound **5**, forms upon loss of the [Tp<sup>tBu,Me</sup>]<sup>−</sup> ligand, which has allowed us to study, for the first time, a well-defined tri-vanadium tetra-nitride motif, where the central V center is supported *only* by bridging nitride ligands, [(Tp<sup>tBu,Me</sup>)V]<sub>2</sub>(μ<sub>4</sub>-VN<sub>4</sub>), thus exhibiting a double-diamond core. This is the first example of a [VN<sub>4</sub>]<sup>8−</sup> analogue of the ubiquitous vanadate ion, [VO<sub>4</sub>]<sup>3−</sup>. We are currently exploring the reactivity of complex **5** since its central V ion could act as a molecular mimic of vanadium nitride surfaces. We are also investigating the reactivity of the terminal V<sup>IV</sup> nitrides **B** and **B-L**.

## ASSOCIATED CONTENT

### Supporting Information

The Supporting Information is available free of charge at <https://pubs.acs.org/doi/10.1021/jacs.2c00276>.

Synthetic procedures, NMR, IR, UV–vis, EPR, HFEPN, SQUID, computational, electrochemical, and X-ray crystallographic data (PDF)

Computational data of coordinates (PDF)

S-SOMO rotation (ZIP)

### Accession Codes

CCDC 1971914–1971922 and 2126109–2126113 contain the supplementary crystallographic data for this paper. These data can be obtained free of charge via [www.ccdc.cam.ac.uk/data\\_request/cif](http://www.ccdc.cam.ac.uk/data_request/cif), or by emailing [data\\_request@ccdc.cam.ac.uk](mailto:data_request@ccdc.cam.ac.uk), or by contacting The Cambridge Crystallographic Data Centre, 12 Union Road, Cambridge CB2 1EZ, UK; fax: +44 1223 336033.

## AUTHOR INFORMATION

### Corresponding Authors

Joshua Telsler – Department of Biological, Physical and Health Sciences, Roosevelt University, Chicago, Illinois 60605, United States; [orcid.org/0000-0003-3307-2556](https://orcid.org/0000-0003-3307-2556); Email: [jtelsler@roosevelt.edu](mailto:jtelsler@roosevelt.edu)

Massimiliano Delferro – Chemical Sciences and Engineering Division, Argonne National Laboratory, Lemont, Illinois 60439, United States; [orcid.org/0000-0002-4443-165X](https://orcid.org/0000-0002-4443-165X); Email: [delferro@anl.gov](mailto:delferro@anl.gov)

Karsten Meyer – Inorganic Chemistry, Department of Chemistry and Pharmacy, Friedrich-Alexander-University Erlangen-Nürnberg (FAU), 91058 Erlangen, Germany; [orcid.org/0000-0002-7844-2998](https://orcid.org/0000-0002-7844-2998); Email: [karsten.meyer@fau.de](mailto:karsten.meyer@fau.de)

Daniel J. Mindiola – Department of Chemistry, University of Pennsylvania, Philadelphia, Pennsylvania 19104, United States; [orcid.org/0000-0001-8205-7868](https://orcid.org/0000-0001-8205-7868); Email: [mindiola@sas.upenn.edu](mailto:mindiola@sas.upenn.edu)

### Authors

Mehrfarshan G. Jafari – Department of Chemistry, University of Pennsylvania, Philadelphia, Pennsylvania 19104, United States; [orcid.org/0000-0001-6807-7520](https://orcid.org/0000-0001-6807-7520)

Dominik Fehn – Inorganic Chemistry, Department of Chemistry and Pharmacy, Friedrich-Alexander-University Erlangen-Nürnberg (FAU), 91058 Erlangen, Germany

Anders Reinholdt – Department of Chemistry, University of Pennsylvania, Philadelphia, Pennsylvania 19104, United States; [orcid.org/0000-0001-6637-8338](https://orcid.org/0000-0001-6637-8338)

Cristina Hernández-Prieto – Department of Chemistry, University of Pennsylvania, Philadelphia, Pennsylvania 19104, United States

Prajay Patel – Chemical Sciences and Engineering Division, Argonne National Laboratory, Lemont, Illinois 60439, United States; [orcid.org/0000-0002-6763-6295](https://orcid.org/0000-0002-6763-6295)

Michael R. Gau – Department of Chemistry, University of Pennsylvania, Philadelphia, Pennsylvania 19104, United States; [orcid.org/0000-0002-4790-6980](https://orcid.org/0000-0002-4790-6980)

Patrick J. Carroll – Department of Chemistry, University of Pennsylvania, Philadelphia, Pennsylvania 19104, United States; [orcid.org/0000-0002-8142-7211](https://orcid.org/0000-0002-8142-7211)

J. Krzystek – National High Magnetic Field Laboratory, Florida State University, Tallahassee, Florida 32310, United States; [orcid.org/0000-0001-6088-1936](https://orcid.org/0000-0001-6088-1936)

Cong Liu – Chemical Sciences and Engineering Division, Argonne National Laboratory, Lemont, Illinois 60439, United States; [orcid.org/0000-0002-2145-5034](https://orcid.org/0000-0002-2145-5034)

Andrew Ozarowski – National High Magnetic Field Laboratory, Florida State University, Tallahassee, Florida 32310, United States; [orcid.org/0000-0001-6225-9796](https://orcid.org/0000-0001-6225-9796)

Complete contact information is available at:  
<https://pubs.acs.org/10.1021/jacs.2c00276>

### Author Contributions

All authors have given approval to the final version of the manuscript.

### Funding

The authors thank the US National Science Foundation (CHE-1464659) and the University of Pennsylvania for financial support of this research. The authors also acknowledge the NIH supplements award 3R01GM118510-03S1 and 3R01GM087605-06S1 and financial support of Vagelos Institute for Energy Sciences and Technology for the purchase of NMR instrument NEO600. A.R. also thanks the Carlsberg Foundation (Grant CF18-0613) and the Independent Research Fund Denmark (grant 9036-00015B) for funding. Part of this work was performed at the National High Magnetic Field Laboratory, which is supported by NSF Cooperative Agreement DMR-1644779 and the State of Florida. EPR studies at Northwestern University were supported by the U.S. Department of Energy (DOE), Office of Science, Basic Energy Sciences (BES), under contract DE-SC0019342 to Prof. Brian M. Hoffman. The theoretical work at Argonne National Laboratory was supported by the U.S. Department of Energy (DOE), Office of Basic Energy Sciences, Division of Chemical Sciences, Geosciences, and Biosciences (CSGB), and Catalysis Science Program, under contract DE-AC02-06CH11357. The calculations were performed using the computational resources provided by the Laboratory Computing Resource Center (LCRC) at Argonne. C.H.-P. also thanks Universidad de Alcalá for funding.

### Notes

The authors declare no competing financial interest.

### ACKNOWLEDGMENTS

On the occasion of the 90th anniversary of his birth, we dedicate this paper to the memory of Swiatoslaw (“Jerry”) Trofimenko (1931–2007), the great Ukrainian-American chemist who

invented the “scorpionate” (pyrazolylborate) ligand. We would also like to thank Prof. Jesper Bendix (Copenhagen University) for the Ligfield software and Prof. Brian M. Hoffman (Northwestern University) for use of EPR/ENDOR spectrometers in his laboratory and helpful comments about vanadium nitrogenase.

### ABBREVIATIONS

Tp <sup>tBu,Me</sup>	hydro-tris(3- <i>tert</i> -butyl-5-methylpyrazol-1-yl)borate
Tp <sup>tBu,tBu</sup>	hydro-tris(3,5-di- <i>tert</i> -butylpyrazol-1-yl)borate
CV	cyclic voltammetry
T <sub>d</sub>	tetrahedral
SP	square planar (four-coordinate)
TBP	trigonal bipyramidal
SP	square pyramidal (five-coordinate)
DMAP	4-dimethylaminopyridine
sc-XRD	single-crystal X-ray diffraction
ENDOR	electron nuclear double resonance
HFEPR	high-frequency and -field electron paramagnetic resonance

### ADDITIONAL NOTE

<sup>a</sup>A homoleptic five-coordinate V<sup>III</sup> complex, [NBu<sub>4</sub>]<sub>2</sub>[V<sup>III</sup>(C<sub>6</sub>F<sub>5</sub>)<sub>5</sub>], has been reported, which has a slightly distorted TBP geometry.<sup>26b</sup> The complex is EPR-silent at X- and Q-bands (in contrast to nearly tetrahedral V<sup>III</sup> in [Li(thf)<sub>4</sub>][V-(C<sub>6</sub>Cl<sub>5</sub>)<sub>4</sub>], which has |D| = 0.513 cm<sup>-1</sup>), so it is likely that its zfs is on the order of several cm<sup>-1</sup>.

### REFERENCES

- (1) (a) Van Tamelen, E. E.; Fechter, R. B.; Schneller, S. W.; Boche, G.; Greeley, R. H.; Akermark, B. Titanium(II) in the fixation-reduction of molecular nitrogen under mild conditions. *J. Am. Chem. Soc.* **1969**, *91*, 1551–1552. (b) Van Tamelen, E. E.; Seeley, D. A.; Schneller, S. W.; Rudler, H.; Cretney, W. Intermediates in the titanocene-promoted fixation-reduction of molecular nitrogen. *J. Am. Chem. Soc.* **1970**, *92*, 5251–5253. (c) Yamamoto, A.; Go, S.; Ookawa, M.; Takahashi, M.; Ikeda, S.; Keii, T. Kinetics and Stoichiometry of Nitrogen Fixation with TiCl<sub>3</sub>-Mg and VCl<sub>3</sub>-Mg in Tetrahydrofuran. *Bull. Chem. Soc. Jpn.* **1972**, *45*, 3110–3117. (d) Chatt, J.; Dilworth, J. R.; Richards, R. L. Recent advances in the chemistry of nitrogen fixation. *Chem. Rev.* **1978**, *78*, 589–625. (e) Laplaza, C. E.; Johnson, M. J. A.; Peters, J. C.; Odom, A. L.; Kim, E.; Cummins, C. C.; George, G. N.; Pickering, I. J. Dinitrogen Cleavage by Three-Coordinate Molybdenum(III) Complexes: Mechanistic and Structural Data I. *J. Am. Chem. Soc.* **1996**, *118*, 8623–8638. (f) Cummins, C. C. Reductive cleavage and related reactions leading to molybdenum-element multiple bonds: new pathways offered by three-coordinate molybdenum(III). *Chem. Commun.* **1998**, 1777–1786. (g) Fryzuk, M. D.; Johnson, S. A. The continuing story of dinitrogen activation. *Coord. Chem. Rev.* **2000**, *200–202*, 379–409. (h) Mindiola, D. J.; Meyer, K.; Cherry, J.-P. F.; Baker, T. A.; Cummins, C. C. Dinitrogen Cleavage Stemming from a Heterodinuclear Niobium/Molybdenum N<sub>2</sub> Complex: New Nitridoniobium Systems Including a Niobazene Cyclic Trimer. *Organometallics* **2000**, *19*, 1622–1624. (i) Tsai, Y.-C.; Cummins, C. C. Base-catalyzed dinitrogen cleavage by molybdenum amides. *Inorg. Chim. Acta* **2003**, *345*, 63–69. (j) MacKay, B. A.; Fryzuk, M. D. Dinitrogen Coordination Chemistry: On the Biomimetic Borderlands. *Chem. Rev.* **2004**, *104*, 385–402. (k) Spencer, L. P.; MacKay, B. A.; Patrick, B. O.; Fryzuk, M. D. Inner-sphere two-electron reduction leads to cleavage and functionalization of coordinated dinitrogen. *Proc. Natl. Acad. Sci. U.S.A.* **2006**, *103*, 17094. (l) Hirotsu, M.; Fontaine, P. P.; Epshteyn, A.; Sita, L. R. Dinitrogen Activation at Ambient Temperatures: New Modes of H<sub>2</sub> and PhSiH<sub>3</sub> Additions for an “End-On-Bridged” [Ta(IV)]<sub>2</sub>(μ-η<sup>1</sup>:η<sup>1</sup>-N<sub>2</sub>) Complex and for the Bis(μ-nitrido) [Ta(V)(μ-N)]<sub>2</sub> Product Derived from Facile N≡N Bond Cleavage. *J. Am. Chem. Soc.* **2007**, *129*,

- 9284–9285. (m) Curley, J. J.; Cook, T. R.; Reece, S. Y.; Müller, P.; Cummins, C. C. Shining Light on Dinitrogen Cleavage: Structural Features, Redox Chemistry, and Photochemistry of the Key Intermediate Bridging Dinitrogen Complex. *J. Am. Chem. Soc.* **2008**, *130*, 9394–9405. (n) Askevold, B.; Nieto, J. T.; Tussupbayev, S.; Diefenbach, M.; Herdtweck, E.; Holthausen, M. C.; Schneider, S. Ammonia formation by metal-ligand cooperative hydrogenolysis of a nitrido ligand. *Nat. Chem.* **2011**, *3*, 532–537. (o) Tran, B. L.; Pinter, B.; Nichols, A. J.; Konopka, F. T.; Thompson, R.; Chen, C.-H.; Krzystek, J.; Ozarowski, A.; Telsler, J.; Baik, M.-H.; Meyer, K.; Mindiola, D. J. A Planar Three-Coordinate Vanadium(II) Complex and the Study of Terminal Vanadium Nitrides from N<sub>2</sub>: A Kinetic or Thermodynamic Impediment to N-N Bond Cleavage? *J. Am. Chem. Soc.* **2012**, *134*, 13035–13045. (p) Hinrichsen, S.; Broda, H.; Gradert, C.; Sönksen, L.; Tuzcek, F. Recent developments in synthetic nitrogen fixation. *Annu. Rep., Sect. A: Inorg. Chem.* **2012**, *108*, 17–47. (q) Tanabe, Y.; Nishibayashi, Y. Developing more sustainable processes for ammonia synthesis. *Coord. Chem. Rev.* **2013**, *257*, 2551–2564. (r) Klopsch, I.; Finger, M.; Würtele, C.; Milde, B.; Werz, D. B.; Schneider, S. Dinitrogen Splitting and Functionalization in the Coordination Sphere of Rhenium. *J. Am. Chem. Soc.* **2014**, *136*, 6881–6883. (s) Silant'ev, G. A.; Förster, M.; Schluschaß, B.; Abbenseth, J.; Würtele, C.; Volkmann, C.; Holthausen, M. C.; Schneider, S. Dinitrogen Splitting Coupled to Protonation. *Angew. Chem., Int. Ed.* **2017**, *56*, 5872–5876. (t) Arashiba, K.; Eizawa, A.; Tanaka, H.; Nakajima, K.; Yoshizawa, K.; Nishibayashi, Y. Catalytic Nitrogen Fixation via Direct Cleavage of Nitrogen-Nitrogen Triple Bond of Molecular Dinitrogen under Ambient Reaction Conditions. *Bull. Chem. Soc. Jpn.* **2017**, *90*, 1111–1118. (u) Burford, R. J.; Fryzuk, M. D. Examining the relationship between coordination mode and reactivity of dinitrogen. *Nat. Rev. Chem.* **2017**, *1*, 0026. (v) Burford, R. J.; Yeo, A.; Fryzuk, M. D. Dinitrogen activation by group 4 and group 5 metal complexes supported by phosphine-amido containing ligand manifolds. *Coord. Chem. Rev.* **2017**, *334*, 84–99. (w) Ishida, Y.; Kawaguchi, H. Reactivity of Group 5 Element Dinitrogen Complexes and N<sub>2</sub>-Derived Nitrides. *Nitrogen Fixation; Topics in Organometallic Chemistry*; Springer: Cham, 2017; Vol. 60. (x) Lindley, B. M.; van Alten, R. S.; Finger, M.; Schendzielorz, F.; Würtele, C.; Miller, A. J. M.; Siewert, I.; Schneider, S. Mechanism of Chemical and Electrochemical N<sub>2</sub> Splitting by a Rhenium Pincer Complex. *J. Am. Chem. Soc.* **2018**, *140*, 7922–7935. (y) Doyle, L. R.; Wooles, A. J.; Jenkins, L. C.; Tuna, F.; McInnes, E. J. L.; Liddle, S. T. Catalytic Dinitrogen Reduction to Ammonia at a Triamidoamine-Titanium Complex. *Angew. Chem., Int. Ed.* **2018**, *57*, 6314–6318. (z) Sekiguchi, Y.; Arashiba, K.; Tanaka, H.; Eizawa, A.; Nakajima, K.; Yoshizawa, K.; Nishibayashi, Y. Catalytic Reduction of Molecular Dinitrogen to Ammonia and Hydrazine Using Vanadium Complexes. *Angew. Chem., Int. Ed.* **2018**, *57*, 9064–9068. (aa) Nishibayashi, Y. Development of catalytic nitrogen fixation using transition metal-dinitrogen complexes under mild reaction conditions. *Dalton Trans.* **2018**, *47*, 11290–11297. (ab) Chen, X.; Zhao, X.; Kong, Z.; Ong, W.-J.; Li, N. Unravelling the electrochemical mechanisms for nitrogen fixation on single transition metal atoms embedded in defective graphitic carbon nitride. *J. Mater. Chem. A* **2018**, *6*, 21941–21948. (ac) Schluschaß, B.; Abbenseth, J.; Demeshko, S.; Finger, M.; Franke, A.; Herwig, C.; Würtele, C.; Ivanovic-Burmazovic, I.; Limberg, C.; Telsler, J.; Schneider, S. Selectivity of tungsten mediated dinitrogen splitting vs. proton reduction. *Chem. Sci.* **2019**, *10*, 10275–10282. (ad) Doyle, L. R.; Wooles, A. J.; Liddle, S. T. Bimetallic Cooperative Cleavage of Dinitrogen to Nitride and Tandem Frustrated Lewis Pair Hydrogenation to Ammonia. *Angew. Chem., Int. Ed.* **2019**, *58*, 6674–6677. (ae) Chalkley, M. J.; Drover, M. W.; Peters, J. C. Catalytic N<sub>2</sub>-to-NH<sub>3</sub> (or -N<sub>2</sub>H<sub>4</sub>) Conversion by Well-Defined Molecular Coordination Complexes. *Chem. Rev.* **2020**, *120*, 5582–5636. (af) Singh, D.; Buratto, W. R.; Torres, J. F.; Murray, L. J. Activation of Dinitrogen by Polynuclear Metal Complexes. *Chem. Rev.* **2020**, *120*, 5517–5581. (ag) Bruch, Q. J.; Connor, G. P.; McMillion, N. D.; Goldman, A. S.; Hasanayn, F.; Holland, P. L.; Miller, A. J. M. Considering Electrocatalytic Ammonia Synthesis via Bimetallic Dinitrogen Cleavage. *ACS Catal.* **2020**, *10*, 10826–10846. (ah) Kim, S.; Loose, F.; Chirik, P. J. Beyond Ammonia: Nitrogen-Element Bond Forming Reactions with Coordinated Dinitrogen. *Chem. Rev.* **2020**, *120*, 5637–5681. (ai) Forrest, S. J. K.; Schluschaß, B.; Yuzik-Klimova, E. Y.; Schneider, S. Nitrogen Fixation via Splitting into Nitrido Complexes. *Chem. Rev.* **2021**, *121*, 6522–6587. (2) (a) Eady, R. Current status of structure function relationships of vanadium nitrogenase. *Coord. Chem. Rev.* **2003**, *237*, 23–30. (b) Hoffman, B. M.; Dean, D. R.; Seefeldt, L. C. Climbing Nitrogenase: Toward a Mechanism of Enzymatic Nitrogen Fixation. *Acc. Chem. Res.* **2009**, *42*, 609–619. (c) Hu, Y.; Lee, C. C.; Ribbe, M. W. Vanadium nitrogenase: A two-hit wonder? *Dalton Trans.* **2012**, *41*, 1118–1127. (d) Varley, J. B.; Wang, Y.; Chan, K.; Studt, F.; Nørskov, J. K. Mechanistic insights into nitrogen fixation by nitrogenase enzymes. *Phys. Chem. Chem. Phys.* **2015**, *17*, 29541–29547. (e) Corić, I.; Holland, P. L. Insight into the Iron-Molybdenum Cofactor of Nitrogenase from Synthetic Iron Complexes with Sulfur, Carbon, and Hydride Ligands. *J. Am. Chem. Soc.* **2016**, *138*, 7200–7211. (f) Seefeldt, L. C.; Yang, Z.-Y.; Lukoyanov, D. A.; Harris, D. F.; Dean, D. R.; Raagei, S.; Hoffman, B. M. Reduction of Substrates by Nitrogenases. *Chem. Rev.* **2020**, *120*, 5082–5106. (g) Jasniowski, A. J.; Lee, C. C.; Ribbe, M. W.; Hu, Y. Reactivity, Mechanism, and Assembly of the Alternative Nitrogenases. *Chem. Rev.* **2020**, *120*, 5107–5157. (h) Yang, Z.-Y.; Jimenez-Vicente, E.; Kallas, H.; Lukoyanov, D. A.; Yang, H.; Martin del Campo, J. S.; Dean, D. R.; Hoffman, B. M.; Seefeldt, L. C. The electronic structure of FeV-cofactor in vanadium-dependent nitrogenase. *Chem. Sci.* **2021**, *12*, 6913–6922. (3) Yang, X.; Nash, J.; Anibal, J.; Dunwell, M.; Kattel, S.; Stavitski, E.; Attenkofer, K.; Chen, J. G.; Yan, Y.; Xu, B. Mechanistic Insights into Electrochemical Nitrogen Reduction Reaction on Vanadium Nitride Nanoparticles. *J. Am. Chem. Soc.* **2018**, *140*, 13387–13391. (4) Choi, D.; Blomgren, G. E.; Kumta, P. N. Fast and Reversible Surface Redox Reaction in Nanocrystalline Vanadium Nitride Supercapacitors. *Adv. Mater.* **2006**, *18*, 1178–1182. (5) (a) Zhao, B. R.; Chen, L.; Luo, H. L.; Jack, M. D.; Mullin, D. P. Superconducting and normal-state properties of vanadium nitride. *Phys. Rev. B: Condens. Matter Mater. Phys.* **1984**, *29*, 6198–6202. (b) Sun, Z.; Zhang, J.; Yin, L.; Hu, G.; Fang, R.; Cheng, H.-M.; Li, F. Conductive porous vanadium nitride/graphene composite as chemical anchor of polysulfides for lithium-sulfur batteries. *Nat. Commun.* **2017**, *8*, 14627. (c) Liu, Y.; Wu, Q.; Liu, L.; Manasa, P.; Kang, L.; Ran, F. Vanadium nitride for aqueous supercapacitors: a topic review. *J. Mater. Chem. A* **2020**, *8*, 8218–8233. (6) Hojo, J.; Iwamoto, O.; Maruyama, Y.; Kato, A. Defect structure, thermal and electrical properties of Ti nitride and V nitride powders. *J. Less-Common Met.* **1977**, *53*, 265–276. (7) (a) Robert, K.; Stiévenard, D.; Deresmes, D.; Douard, C.; Iadecola, A.; Troadec, D.; Simon, P.; Nuns, N.; Marinova, M.; Huvé, M.; Roussel, P.; Brousse, T.; Lethien, C. Novel insights into the charge storage mechanism in pseudocapacitive vanadium nitride thick films for high-performance on-chip micro-supercapacitors. *Energy Environ. Sci.* **2020**, *13*, 949–957. (b) Zhou, X.; Chen, H.; Shu, D.; He, C.; Nan, J. Study on the electrochemical behavior of vanadium nitride as a promising supercapacitor material. *J. Phys. Chem. Solids* **2009**, *70*, 495–500. (c) Zhou, X.; Shang, C.; Gu, L.; Dong, S.; Chen, X.; Han, P.; Li, L.; Yao, J.; Liu, Z.; Xu, H.; Zhu, Y.; Cui, G. Mesoporous Coaxial Titanium Nitride-Vanadium Nitride Fibers of Core-shell Structures for High-Performance Supercapacitors. *ACS Appl. Mater. Interfaces* **2011**, *3*, 3058–3063. (d) Ghimbeu, C. M.; Raymundo-Piñero, E.; Fioux, P.; Béguin, F.; Vix-Guterl, C. Vanadium nitride/carbon nanotube nanocomposites as electrodes for supercapacitors. *J. Mater. Chem.* **2011**, *21*, 13268–13275. (e) Lu, X.; Yu, M.; Zhai, T.; Wang, G.; Xie, S.; Liu, T.; Liang, C.; Tong, Y.; Li, Y. High Energy Density Asymmetric Quasi-Solid-State Supercapacitor Based on Porous Vanadium Nitride Nanowire Anode. *Nano Lett.* **2013**, *13*, 2628–2633. (f) Zhu, C.; Yang, P.; Chao, D.; Wang, X.; Zhang, X.; Chen, S.; Tay, B. K.; Huang, H.; Zhang, H.; Mai, W.; Fan, H. J. All Metal Nitrides Solid-State Asymmetric Supercapacitors. *Adv. Mater.* **2015**, *27*, 4566–4571. (g) Xu, Y.; Wang, J.; Shen, L.; Dou, H.; Zhang, X. One-Dimensional Vanadium Nitride Nanofibers Fabricated by Electrospinning for Supercapacitors. *Electrochim. Acta* **2015**, *173*, 680–686. (h) Gao, B.;

- Li, X.; Guo, X.; Zhang, X.; Peng, X.; Wang, L.; Fu, J.; Chu, P. K.; Huo, K. Nitrogen-Doped Carbon Encapsulated Mesoporous Vanadium Nitride Nanowires as Self-Supported Electrodes for Flexible All-Solid-State Supercapacitors. *Adv. Mater. Interfaces* **2015**, *2*, 1500211. (i) Bi, W.; Hu, Z.; Li, X.; Wu, C.; Wu, J.; Wu, Y.; Xie, Y. Metallic mesocrystal nanosheets of vanadium nitride for high-performance all-solid-state pseudocapacitors. *Nano Res.* **2015**, *8*, 193–200. (j) Yan, Y.; Li, B.; Guo, W.; Pang, H.; Xue, H. Vanadium based materials as electrode materials for high performance supercapacitors. *J. Power Sources* **2016**, *329*, 148–169. (k) Liu, Y.; Liu, L.; Kong, L.; Kang, L.; Ran, F. Supercapacitor Electrode Based on Nano-Vanadium Nitride Incorporated on Porous Carbon Nanospheres Derived from Ionic Amphiphilic Block Copolymers & Vanadium-Contained Ion Assembly Systems. *Electrochim. Acta* **2016**, *211*, 469–477. (l) Hanumantha, P. J.; Datta, M. K.; Kadakia, K.; Okoli, C.; Patel, P.; Kumta, P. N. Vanadium nitride supercapacitors: Effect of Processing Parameters on electrochemical charge storage behavior. *Electrochim. Acta* **2016**, *207*, 37–47. (m) Balamurugan, J.; Karthikeyan, G.; Thanh, T. D.; Kim, N. H.; Lee, J. H. Facile synthesis of vanadium nitride/nitrogen-doped graphene composite as stable high performance anode materials for supercapacitors. *J. Power Sources* **2016**, *308*, 149–157. (n) Wang, B.; Chen, Z.; Lu, G.; Wang, T.; Ge, Y. Exploring electrolyte preference of vanadium nitride supercapacitor electrodes. *Mater. Res. Bull.* **2016**, *76*, 37–40. (o) Wu, Y.; Ran, F. Vanadium nitride quantum dot/nitrogen-doped microporous carbon nanofibers electrode for high-performance supercapacitors. *J. Power Sources* **2017**, *344*, 1–10. (p) Achour, A.; Lucio-Porto, R.; Chaker, M.; Arman, A.; Ahmadpourian, A.; Soussou, M. A.; Boujtita, M.; Le Brizoual, L.; Djouadi, M. A.; Brousse, T. Titanium vanadium nitride electrode for micro-supercapacitors. *Electrochem. Commun.* **2017**, *77*, 40–43. (q) Venkateshalu, S.; Cherusseri, J.; Karnan, M.; Kumar, K. S.; Kollu, P.; Sathish, M.; Thomas, J.; Jeong, S. K.; Grace, A. N. New Method for the Synthesis of 2D Vanadium Nitride (MXene) and Its Application as a Supercapacitor Electrode. *ACS Omega* **2020**, *5*, 17983–17992.
- (8) (a) Willing, W.; Christophersen, R.; Müller, U.; Dehnicke, K.  $\text{VNCl}_2(\text{Pyridin})_2$  Synthese, IR-Spektrum und Kristallstruktur. *Z. Anorg. Allg. Chem.* **1987**, *555*, 16–22. (b) Critchlow, S. C.; Lerchen, M. E.; Smith, R. C.; Doherty, N. M. Vanadium nitride linear chain polymers and monomers. Synthesis and structures of  $[\text{V}(\mu\text{-N})\text{Cl}_2(\text{py})_2]_\infty$  and  $\text{V}(\text{N})\text{Cl}_2(\text{quin})_2$ . *J. Am. Chem. Soc.* **1988**, *110*, 8071–8075. (c) Hills, A.; Hughes, D. L.; Leigh, G. J.; Prieto-Alcón, R. Compounds with vanadium-nitrogen and vanadium-oxygen multiple bonds. *J. Chem. Soc., Dalton Trans.* **1993**, 3609–3617. (d) Song, J.-L.; Gambarotta, S. Preparation, Characterization, and Reactivity of a Diamagnetic Vanadium Nitride. *Chem.—Eur. J.* **1996**, *2*, 1258–1263. (e) Henderson, R. A.; Janas, Z.; Jerzykiewicz, L. B.; Richards, R. L.; Sobota, P. Vanadium phenoxide complexes with oxide, nitride or hydrazide co-ligands: preparation and crystal structures of  $[\text{V}(\text{OC}_6\text{H}_5\text{Pr}^i_2\text{-}2,6)_3\text{N}(\text{Li}(\text{C}_4\text{H}_8\text{O})_3)]$ ,  $[\{\text{VO}_2(\text{OC}_6\text{H}_5\text{Pr}^i_2\text{-}2,6)_2\}_2\{\mu\text{-Li}(\text{C}_4\text{H}_8\text{O})_2\}_2]$  and  $[\text{V}(\text{NNMe}_2)(\text{OC}_6\text{H}_5\text{Pr}^i_2\text{-}2,6)_3]$ . *Inorg. Chim. Acta* **1999**, *285*, 178–183. (f) Brask, J. K.; Durà-Vilà, V.; Diaconescu, P. L.; Cummins, C. C. Vanadium nitride functionalization and denitrogenation by carbon disulfide and dioxide. *Chem. Commun.* **2002**, 902–903. (g) Johnson, C. E.; Kysor, E. A.; Findlater, M.; Jasinski, J. P.; Metell, A. S.; Queen, J. W.; Abernethy, C. D. The synthesis and characterization of  $[\text{IMesH}]^+[(\eta^3\text{-C}_5\text{H}_5)\text{V}(\text{N})\text{Cl}_2]^-$ : An anionic vanadium(V) complex with a terminal nitrido ligand. *Dalton Trans.* **2010**, *39*, 3482–3488. (h) Tran, B. L.; Pink, M.; Gao, X.; Park, H.; Mindiola, D. J. Low-Coordinate and Neutral Nitrido Complexes of Vanadium. *J. Am. Chem. Soc.* **2010**, *132*, 1458–1459. (i) Tran, B. L.; Singhal, M.; Park, H.; Lam, O. P.; Pink, M.; Krzystek, J.; Ozarowski, A.; Telsler, J.; Meyer, K.; Mindiola, D. J. Reactivity Studies of a Masked Three-Coordinate Vanadium(II) Complex. *Angew. Chem., Int. Ed.* **2010**, *49*, 9871–9875. (j) Groysman, S.; Villagrán, D.; Freedman, D. E.; Nocera, D. G. Dinitrogen binding at vanadium in a tris(alkoxide) ligand environment. *Chem. Commun.* **2011**, *47*, 10242–10244. (k) Tran, B. L.; Krzystek, J.; Ozarowski, A.; Chen, C. H.; Pink, M.; Karty, J. A.; Telsler, J.; Meyer, K.; Mindiola, D. J. Formation and Reactivity of the Terminal Vanadium Nitride Functionality. *Eur. J. Inorg. Chem.* **2013**, *2013*, 3916–3929. (l) Ishida, Y.; Kawaguchi, H. Nitrogen Atom Transfer from a Dinitrogen-Derived Vanadium Nitride Complex to Carbon Monoxide and Isocyanide. *J. Am. Chem. Soc.* **2014**, *136*, 16990–16993. (m) Thompson, R.; Tran, B. L.; Ghosh, S.; Chen, C.-H.; Pink, M.; Gao, X.; Carroll, P. J.; Baik, M.-H.; Mindiola, D. J. Addition of Si-H and B-H Bonds and Redox Reactivity Involving Low-Coordinate Nitrido-Vanadium Complexes. *Inorg. Chem.* **2015**, *54*, 3068–3077.
- (9) (a) Abernethy, C. D.; Bottomley, F.; Decken, A.; Cameron, T. S. Preparation and Properties of a Closo Nitride Cluster, the Cubane  $[(\eta\text{-C}_5\text{Me}_5)\text{V}(\mu_3\text{-N})_4]$ . *Organometallics* **1996**, *15*, 1758–1759. (b) Clent-smith, G. K. B.; Bates, V. M. E.; Hitchcock, P. B.; Cloke, F. G. N. Reductive Cleavage of Dinitrogen by a Vanadium Diamidoamine Complex: the Molecular Structures of  $[\text{V}(\text{Me}_3\text{SiN}\{\text{CH}_2\text{CH}_2\text{NSiMe}_3\}_2)(\mu\text{-N})_2]$  and  $[\text{V}(\text{Me}_3\text{SiN}\{\text{CH}_2\text{CH}_2\text{NSiMe}_3\}_2)(\mu\text{-N})_2]$ . *J. Am. Chem. Soc.* **1999**, *121*, 10444–10445.
- (10) Ballhausen, C. J.; Gray, H. B. The Electronic Structure of the Vanadyl Ion. *Inorg. Chem.* **1962**, *1*, 111–122.
- (11) (a) Rychcik, M.; Skyllas-Kazacos, M. Characteristics of a new all-vanadium redox flow battery. *J. Power Sources* **1988**, *22*, 59–67. (b) Galiote, N. A.; Camargo, M. N. L.; Iost, R. M.; Crespilho, F.; Huguenin, F. Effects of Self-Assembled Materials Prepared from  $\text{V}_2\text{O}_5$  for Lithium Ion Electroinsertion. *Langmuir* **2011**, *27*, 12209–12217. (c) Lala, N. L.; Jose, R.; Yusoff, M. M.; Ramakrishna, S. Continuous tubular nanofibers of vanadium pentoxide by electrospinning for energy storage devices. *J. Nanopart. Res.* **2012**, *14*, 1201. (d) Bai, M.-H.; Bian, L.-J.; Song, Y.; Liu, X.-X. Electrochemical Codeposition of Vanadium Oxide and Polypyrrole for High-Performance Supercapacitor with High Working Voltage. *ACS Appl. Mater. Interfaces* **2014**, *6*, 12656–12664.
- (12) (a) Rehder, D. The Bioinorganic Chemistry of Vanadium. *Angew. Chem., Int. Ed. Engl.* **1991**, *30*, 148–167. (b) Smith, T. S.; LoBrutto, R.; Pecoraro, V. L. Paramagnetic spectroscopy of vanadyl complexes and its applications to biological systems. *Coord. Chem. Rev.* **2002**, *228*, 1–18. (c) Frank, P.; Carlson, E. J.; Carlson, R. M. K.; Hedman, B.; Hodgson, K. O. The uptake and fate of vanadyl ion in ascidian blood cells and a detailed hypothesis for the mechanism and location of biological vanadium reduction. A visible and X-ray absorption spectroscopic study. *J. Inorg. Biochem.* **2008**, *102*, 809–823.
- (13) (a) Gordon, R. G. Recent Advances in the CVD of Metal Nitrides and Oxides. *MRS Online Proc. Libr.* **1993**, *335*, 9–19. (b) Hoffman, D. M. Chemical vapour deposition of nitride thin films. *Polyhedron* **1994**, *13*, 1169–1179. (c) Valade, L.; Choukroun, R.; Cassoux, P.; Teyssandier, F.; Poirier, L.; Ducarroir, M.; Feuer, R.; Bonnefond, P.; Maury, F. Single-source precursors for the chemical vapor deposition of titanium and vanadium carbide and nitride. In *The Chemistry of Transition Metal Carbides and Nitrides*; Oyama, S. T., Ed.; Springer Netherlands: Dordrecht, 1996; pp 290–310. (d) Kim, H. Atomic layer deposition of metal and nitride thin films: Current research efforts and applications for semiconductor device processing. *J. Vac. Sci. Technol., B: Microelectron. Nanometer Struct.—Process., Meas., Phenom.* **2003**, *21*, 2231–2261. (e) Kafizas, A.; Carmalt, C. J.; Parkin, I. P. CVD and precursor chemistry of transition metal nitrides. *Coord. Chem. Rev.* **2013**, *257*, 2073–2119.
- (14) Petrov, P. A.; Smolentsev, A. I.; Bogomyakov, A. S.; Konchenko, S. N. Novel vanadium complexes supported by a bulky tris(pyrazolyl)-borate ligand. *Polyhedron* **2017**, *129*, 60–64.
- (15) (a) Murtuza, S.; Casagrande, O. L.; Jordan, R. F. Ethylene Polymerization Behavior of Tris(pyrazolyl)borate Titanium(IV) Complexes. *Organometallics* **2002**, *21*, 1882–1890. (b) Lee, H.; Jordan, R. F. Unusual Reactivity of Tris(pyrazolyl)borate Zirconium Benzyl Complexes. *J. Am. Chem. Soc.* **2005**, *127*, 9384–9385. (c) Biagini, P.; Calderazzo, F.; Marchetti, F.; Romano, A. M.; Spera, S. Synthesis and structural characterization of sterically crowded hydridotris(pyrazolyl)borate complexes: Unusual double 1,2-borotropic shift at a titanium centre. *J. Organomet. Chem.* **2006**, *691*, 4172–4180.
- (16) (a) Trofimenko, S.; Calabrese, J. C.; Kochi, J. K.; Wolowicz, S.; Hulsbergen, F. B.; Reedijk, J. Spectroscopic analysis, coordination geometry, and x-ray structures of nickel(II) compounds with sterically demanding tris(pyrazolyl)borate ligands and azide or (thio)cyanate

- anions. Crystal and molecular structures of bis[( $\mu$ -thiocyanato-N,S)(hydrotris(3-isopropyl-4-bromopyrazol-1-yl)borato)nickel(II)]-3-heptane and (thiocyanato-N)(hydrotris(3-tert-butyl-5-methylpyrazol-1-yl)borato)nickel(II). *Inorg. Chem.* **1992**, *31*, 3943–3950.
- (b) López, C.; Sanz, D.; Claramunt, R. M.; Trofimenko, S.; Elguero, J. An  $^1\text{H}$  and  $^{13}\text{C}$  NMR spectroscopic study of the structure of potassium and thallium salts of tris- and tetrakis-(pyrazol-1-yl) borates in solution. Some  $^{13}\text{C}$ – $^{11}\text{B}$  and  $^{13}\text{C}$ – $^{205}\text{Tl}$  residual coupling constants. *J. Organomet. Chem.* **1995**, *503*, 265–276. (c) Trofimenko, S. Scorpionates: genesis, milestones, prognosis. *Polyhedron* **2004**, *23*, 197–203.
- (17) (a) Egan, J. W.; Haggerty, B. S.; Rheingold, A. L.; Sendlinger, S. C.; Theopold, K. H. Crystal structure of a side-on superoxo complex of cobalt and hydrogen abstraction by a reactive terminal oxo ligand. *J. Am. Chem. Soc.* **1990**, *112*, 2445–2446. (b) Kersten, J. L.; Kucharczyk, R. R.; Yap, G. P. A.; Rheingold, A. L.; Theopold, K. H.  $[(\text{Tp}^{\text{t-Bu,Me}})\text{CrR}]$ : A New Class of Mononuclear, Coordinatively Unsaturated Chromium(II) Alkyls with cis-Divacant Octahedral Structure. *Chem.—Eur. J.* **1997**, *3*, 1668–1674. (c) Hess, A.; Hörz, M. R.; Liable-Sands, L. M.; Lindner, D. C.; Rheingold, A. L.; Theopold, K. H. Insertion of  $\text{O}_2$  into a Chromium–Phenyl Bond: Mechanism of Formation of the Paramagnetic  $d^2$  Oxo Complex  $[\text{Tp}^{\text{t-Bu,Me}}\text{Cr}^{\text{IV}}(\text{O})\text{OPh}]$ . *Angew. Chem., Int. Ed.* **1999**, *38*, 166–168. (d) Jewson, J. D.; Liable-Sands, L. M.; Yap, G. P. A.; Rheingold, A. L.; Theopold, K. H. Paramagnetic Alkyl, Hydride, and Alkene Complexes of the  $\text{Tp}^{\text{t-Bu,Me}}\text{Co}$  Moiety. *Organometallics* **1999**, *18*, 300–305. (e) Thyagarajan, S.; Incarvito, C. D.; Rheingold, A. L.; Theopold, K. H. Formation and reactivity of a cobalt(II) hydroperoxide intermediate. *Chem. Commun.* **2001**, 2198–2199. (f) Qin, K.; Incarvito, C. D.; Rheingold, A. L.; Theopold, K. H. A Structurally Characterized Chromium(III) Superoxide Complex Features “Side-on” Bonding. *Angew. Chem., Int. Ed.* **2002**, *41*, 2333–2335. (g) Qin, K.; Incarvito, C. D.; Rheingold, A. L.; Theopold, K. H. Hydrogen Atom Abstraction by a Chromium(IV) Oxo Complex Derived from  $\text{O}_2$ . *J. Am. Chem. Soc.* **2002**, *124*, 14008–14009. (h) Cramer, C. J.; Tolman, W. B.; Theopold, K. H.; Rheingold, A. L. Variable character of O—O and M—O bonding in side-on ( $\eta^2$ ) 1:1 metal complexes of  $\text{O}_2$ . *Proc. Natl. Acad. Sci. U.S.A.* **2003**, *100*, 3635. (i) Thyagarajan, S.; Shay, D. T.; Incarvito, C. D.; Rheingold, A. L.; Theopold, K. H. Intramolecular C–H Activation by Inferred Terminal Cobalt Imido Intermediates. *J. Am. Chem. Soc.* **2003**, *125*, 4440–4441. (j) Thyagarajan, S.; Incarvito, C. D.; Rheingold, A. L.; Theopold, K. H. In pursuit of a stable peroxyimide complex— $\text{NO}_x$  ( $x=1-3$ ) derivatives of  $\text{Tp}^{\text{t-Bu,MeCo}}$ . *Inorg. Chim. Acta* **2003**, *345*, 333–339. (k) Shay, D. T.; Yap, G. P. A.; Zakharov, L. N.; Rheingold, A. L.; Theopold, K. H. Intramolecular C:H Activation by an Open-Shell Cobalt(III) Imido Complex. *Angew. Chem., Int. Ed.* **2005**, *44*, 1508–1510. (l) Jové, F. A.; Pariya, C.; Scoblete, M.; Yap, G. P. A.; Theopold, K. H. A Family of Four-Coordinate Iron(II) Complexes Bearing the Sterically Hindered Tris(pyrazolyl)borato Ligand  $\text{Tp}^{\text{t-Bu,Me}}$ . *Chem.—Eur. J.* **2011**, *17*, 1310–1318. (m) Akturk, E. S.; Yap, G. P. A.; Theopold, K. H. Mechanism-based design of labile precursors for chromium(i) chemistry. *Chem. Commun.* **2015**, *51*, 15402–15405. (n) Akturk, E. S.; Yap, G. P. A.; Theopold, K. H. Dioxygen Activation by Non-Adiabatic Oxidative Addition to a Single Metal Center. *Angew. Chem., Int. Ed.* **2015**, *54*, 14974–14977. (o) Cummins, D. C.; Yap, G. P. A.; Theopold, K. H. Scorpionates of the “Tetrahedral Enforcer” Variety as Ancillary Ligands for Dinitrogen Complexes of First Row Transition Metals (Cr–Co). *Eur. J. Inorg. Chem.* **2016**, *2016*, 2349–2356.
- (18) (a) Alsfasser, R.; Trofimenko, S.; Looney, A.; Parkin, G.; Vahrenkamp, H. A mononuclear zinc hydroxide complex stabilized by a highly substituted tris(pyrazolyl)hydroborato ligand: analogies with the enzyme carbonic anhydrase. *Inorg. Chem.* **1991**, *30*, 4098–4100. (b) Looney, A.; Han, R.; McNeill, K.; Parkin, G. Tris(pyrazolyl)-hydroboratozinc hydroxide complexes as functional models for carbonic anhydrase: on the nature of the bicarbonate intermediate. *J. Am. Chem. Soc.* **1993**, *115*, 4690–4697. (c) Looney, A.; Saleh, A.; Zhang, Y.; Parkin, G. Tris(pyrazolyl)hydroborato Complexes of Cadmium: A Bidentate Nitrate Derivative and Its Relevance to Carbonic Anhydrase Activity. *Inorg. Chem.* **1994**, *33*, 1158–1164. (d) Yoon, K.; Parkin, G. Tris(3-*t*-butyl-5-methylpyrazolyl)hydroborato derivatives of copper and thallium: The structural influence of a 5-methyl substituent. *Polyhedron* **1995**, *14*, 811–821. (e) Kuchta, M. C.; Parkin, G. Terminal Chalcogenido Complexes of Gallium Supported by Tris(3,5-di-*tert*-butylpyrazolyl)hydroborato Ligand:  $[\text{Tp}^{\text{t-Bu,Me}}]\text{GaE}$  ( $E = \text{Se}, \text{Te}$ ). *Inorg. Chem.* **1997**, *36*, 2492–2493. (f) Ghosh, P.; Desrosiers, P. J.; Parkin, G. Chemical Shift Anisotropy as a Mechanism for Modulating Apparent  $J_{\text{Ti-H}}$  and  $J_{\text{Ti-C}}$  Coupling Constants in Tris-(pyrazolyl)hydroborato Thallium Complexes. *J. Am. Chem. Soc.* **1998**, *120*, 10416–10422. (g) Bergquist, C.; Parkin, G. Modeling the Catalytic Cycle of Liver Alcohol Dehydrogenase: Synthesis and Structural Characterization of a Four-Coordinate Zinc Ethoxide Complex and Determination of Relative Zn–OR versus Zn–OH Bond Energies. *Inorg. Chem.* **1999**, *38*, 422–423. (h) Bergquist, C.; Parkin, G. Protonation of the Hydroxide Ligand in a Synthetic Analogue of Carbonic Anhydrase,  $[\text{Tp}^{\text{t-Bu,Me}}]\text{ZnOH}$ : Inhibition of Reactivity Towards  $\text{CO}_2$ . *J. Am. Chem. Soc.* **1999**, *121*, 6322–6323. (i) Bergquist, C.; Storrie, H.; Koutcher, L.; Bridgewater, B. M.; Friesner, R. A.; Parkin, G. Factors Influencing the Thermodynamics of Zinc Alkoxide Formation by Alcoholysis of the Terminal Hydroxide Complex,  $[\text{Tp}^{\text{t-Bu,Me}}]\text{ZnOH}$ : An Experimental and Theoretical Study Relevant to the Mechanism of Action of Liver Alcohol Dehydrogenase. *J. Am. Chem. Soc.* **2000**, *122*, 12651–12658. (j) Bergquist, C.; Fillebeen, T.; Morlok, M. M.; Parkin, G. Protonation and Reactivity towards Carbon Dioxide of the Mononuclear Tetrahedral Zinc and Cobalt Hydroxide Complexes,  $[\text{Tp}^{\text{t-Bu,Me}}]\text{ZnOH}$  and  $[\text{Tp}^{\text{t-Bu,Me}}]\text{CoOH}$ : Comparison of the Reactivity of the Metal Hydroxide Function in Synthetic Analogues of Carbonic Anhydrase. *J. Am. Chem. Soc.* **2003**, *125*, 6189–6199. (k) Sattler, W.; Parkin, G. Low temperature NMR spectroscopic investigation of a zinc bicarbonate compound: Thermodynamics of bicarbonate formation by insertion of  $\text{CO}_2$  into the zinc hydroxide bond of  $[\text{Tp}^{\text{t-Bu,Me}}]\text{ZnOH}$ . *Polyhedron* **2012**, *32*, 41–48. (l) Chakrabarti, N.; Sattler, W.; Parkin, G. Structural characterization of tris(pyrazolyl)hydroborato and tris(2-pyridylthio)methyl lithium compounds: Lithium in uncommon trigonal pyramidal and trigonal monopyramidal coordination environments. *Polyhedron* **2013**, *58*, 235–246. (m) Rauch, M.; Rong, Y.; Sattler, W.; Parkin, G. Synthesis of a terminal zinc hydride compound,  $[\text{Tp}^{\text{t-Bu,Me}}]\text{ZnH}$ , from a hydroxide derivative,  $[\text{Tp}^{\text{t-Bu,Me}}]\text{ZnOH}$ : Interconversions with the fluoride complex,  $[\text{Tp}^{\text{t-Bu,Me}}]\text{ZnF}$ . *Polyhedron* **2016**, *103*, 135–140. (n) Rauch, M.; Rucolo, S.; Mester, J. P.; Rong, Y.; Parkin, G. Synthesis, structure and reactivity of a terminal magnesium fluoride compound,  $[\text{Tp}^{\text{t-Bu,Me}}]\text{MgF}$ : hydrogen bonding, halogen bonding and C–F bond formation. *Chem. Sci.* **2016**, *7*, 142–149.
- (19) (a) Morissette, M.; Haufe, S.; McDonald, R.; Ferrence, G. M.; Takats, J. Steric saturation of the ytterbium coordination environment:  $(\text{Tp}^{\text{t-Bu,Me}})\text{Yb}(\text{OMe})_2$ , a four coordinate, monomeric, base-free divalent lanthanide complex, its solvation with tetrahydrofuran, and comparison to the  $\beta$ -diketonate complex,  $(\text{Tp}^{\text{t-Bu,Me}})\text{Yb}(\text{dpm})$ . *Polyhedron* **2004**, *23*, 263–271. (b) Ferrence, G. M.; Arduengo, A. J.; Jockisch, A.; Kim, H.-J.; McDonald, R.; Takats, J. Reaction of tetramethylimidazol-2-ylidene with  $(\text{Tp}^{\text{t-Bu,Me}})\text{YbE}(\text{thf})$  ( $E = \text{I}, \text{CH}_2\text{SiMe}_3$ ): simple adduct and a hydrocarbyl tethered carbene ligand. *J. Alloys Compd.* **2006**, *418*, 184–188. (c) Cheng, J.; Saliu, K.; Kiel, G. Y.; Ferguson, M. J.; McDonald, R.; Takats, J. Scorpionate-Supported Dialkyl and Dihydride Lanthanide Complexes: Ligand- and Solvent-Dependent Cluster Hydride Formation. *Angew. Chem., Int. Ed.* **2008**, *47*, 4910–4913. (d) Cheng, J.; Takats, J.; Ferguson, M. J.; McDonald, R. Heteroleptic Tm(II) Complexes: One More Success for Trofimenko’s Scorpionates. *J. Am. Chem. Soc.* **2008**, *130*, 1544–1545. (e) Saliu, K. O.; Maunder, G. H.; Ferguson, M. J.; Sella, A.; Takats, J. Synthesis and structure of heteroleptic ytterbium (II) tetrahydroborate complexes. *Inorg. Chim. Acta* **2009**, *362*, 4616–4622. (f) Zhang, X. W.; Maunder, G. H.; Giessmann, S.; MacDonald, R.; Ferguson, M. J.; Bond, A. H.; Rogers, R. D.; Sella, A.; Takats, J. Stable heteroleptic complexes of divalent lanthanides with bulky pyrazolylborate ligands—iodides, hydrocarbyls and triethylborohydrides. *Dalton Trans.* **2011**, *40*, 195–210.
- (20) (a) Litlabø, R.; Zimmermann, M.; Saliu, K.; Takats, J.; Törnroos, K. W.; Anwander, R. A Rare-Earth Metal Variant of the Tebbe Reagent.

- Angew. Chem., Int. Ed.* **2008**, *47*, 9560–9564. (b) Zimmermann, M.; Takats, J.; Kiel, G.; Törnroos, K. W.; Anwender, R. Ln(III) methyl and methylenedene complexes stabilized by a bulky hydrotris(pyrazolyl)-borate ligand. *Chem. Commun.* **2008**, 612–614. (c) Litlabø, R.; Saliu, K.; Ferguson, M. J.; McDonald, R.; Takats, J.; Anwender, R. Monomeric Tetraalkylaluminates of Divalent Ytterbium Stabilized by a Bulky Tris(pyrazolyl)borate Ligand. *Organometallics* **2009**, *28*, 6750–6754. (d) Zimmermann, M.; Litlabø, R.; Törnroos, K. W.; Anwender, R. “Metastable” Lu(GaMe<sub>4</sub>), Reacts Like Masked [LuMe<sub>3</sub>]: Synthesis of an Unsolvated Lanthanide Dimethyl Complex. *Organometallics* **2009**, *28*, 6646–6649. (e) Schädle, D.; Meermann-Zimmermann, M.; Schädle, C.; Maichle-Mössmer, C.; Anwender, R. Rare-Earth Metal Complexes with Terminal Imido Ligands. *Eur. J. Inorg. Chem.* **2015**, *2015*, 1334–1339. (f) Schädle, D.; Maichle-Mössmer, C.; Schädle, C.; Anwender, R. Rare-Earth-Metal Methyl, Amide, and Imide Complexes Supported by a Superbulky Scorpionate Ligand. *Chem.—Eur. J.* **2015**, *21*, 662–670. (g) Wolf, B. M.; Stuhl, C.; Maichle-Mössmer, C.; Anwender, R. Dimethylcalcium. *J. Am. Chem. Soc.* **2018**, *140*, 2373–2383. (h) Wolf, B. M.; Stuhl, C.; Maichle-Mössmer, C.; Anwender, R. Calcium Tetraalkylaluminate and Tetramethylgallate Complexes Supported by the Bulky Scorpionate Ligand Tp<sup>tBu,Me</sup>. *Organometallics* **2019**, *38*, 1614–1621. (i) Birkelbach, V. M.; Thim, R.; Stuhl, C.; Maichle-Mössmer, C.; Anwender, R. Potential Precursors for Terminal Methylenedene Rare-Earth-Metal Complexes Supported by a Superbulky Tris(pyrazolyl)borato Ligand. *Chem.—Eur. J.* **2019**, *25*, 14711–14720. (j) Birkelbach, V. M.; Stuhl, C.; Maichle-Mössmer, C.; Anwender, R. Mixed Methyl Aryloxy Rare-Earth-Metal Complexes Stabilized by a Superbulky Tris(pyrazolyl)borato Ligand. *Organometallics* **2019**, *38*, 4485–4496.
- (21) (a) Krzystek, J.; Swenson, D. C.; Zvyagin, S. A.; Smirnov, D.; Ozarowski, A.; Telsler, J. Cobalt(II) “Scorpionate” Complexes as Models for Cobalt-Substituted Zinc Enzymes: Electronic Structure Investigation by High-Frequency and -Field Electron Paramagnetic Resonance Spectroscopy. *J. Am. Chem. Soc.* **2010**, *132*, 5241–5253. (b) Kumar, M.; Papish, E. T.; Zeller, M.; Hunter, A. D. Zinc complexes of Tz<sup>R,Me</sup> with O and S donors reveal differences between Tp and Tz ligands: acid stability and binding to H or an additional metal (Tz<sup>R,Me</sup> = tris(3-R-5-methyl-1,2,4-triazolyl)borate; R = Ph, tBu). *Dalton Trans.* **2011**, *40*, 7517–7533. (c) Kumar, M.; Dixon, N. A.; Merkle, A. C.; Zeller, M.; Lehnert, N.; Papish, E. T. Hydrotris(triazolyl)borate Complexes as Functional Models for Cu Nitrite Reductase: The Electronic Influence of Distal Nitrogens. *Inorg. Chem.* **2012**, *51*, 7004–7006. (d) Porter, T. R.; Captao, D.; Kaminsky, W.; Qian, Z.; Mayer, J. M. Synthesis, Radical Reactivity, and Thermochemistry of Monomeric Cu(II) Alkoxide Complexes Relevant to Cu/Radical Alcohol Oxidation Catalysis. *Inorg. Chem.* **2016**, *55*, 5467–5475. (e) Reinholdt, A.; Jafari, M. G.; Sandoval-Pauker, C.; Ballester-Martinez, E.; Gau, M. R.; Driess, M.; Pinter, B.; Mindiola, D. J. Phosphorus and Arsenic Atom Transfer to Isocyanides to Form  $\pi$ -Backbonding Cyanophosphide and Cyanoarsenide Titanium Complexes. *Angew. Chem., Int. Ed.* **2021**, *60*, 17595–17600.
- (22) Trofimenko, S. Recent advances in poly(pyrazolyl)borate (scorpionate) chemistry. *Chem. Rev.* **1993**, *93*, 943–980.
- (23) Addison, A. W.; Rao, T. N.; Reedijk, J.; van Rijn, J.; Verschoor, G. C. Synthesis, structure, and spectroscopic properties of copper(II) compounds containing nitrogen-sulphur donor ligands; the crystal and molecular structure of aqua[1,7-bis(N-methylbenzimidazol-2'-yl)-2,6-dithiaheptane]copper(II) perchlorate. *J. Chem. Soc., Dalton Trans.* **1984**, 1349–1356.
- (24) Krzystek, J.; Zvyagin, S. A.; Ozarowski, A.; Trofimenko, S.; Telsler, J. Tunable-frequency high-field electron paramagnetic resonance. *J. Magn. Reson.* **2006**, *178*, 174–183.
- (25) (a) Beaulac, R.; Tregenna-Piggott, P. L. W.; Barra, A.-L.; Weihe, H.; Luneau, D.; Reber, C. The Electronic Ground State of [V(urea)<sub>6</sub>]<sup>3+</sup> Probed by NIR Luminescence, Electronic Raman, and High-Field EPR Spectroscopies. *Inorg. Chem.* **2006**, *45*, 3399–3407. (b) Van Stappen, C.; Maganas, D.; DeBeer, S.; Bill, E.; Neese, F. Investigations of the Magnetic and Spectroscopic Properties of V(III) and V(IV) Complexes. *Inorg. Chem.* **2018**, *57*, 6421–6438.
- (26) (a) Alonso, P. J.; Forniés, J.; García-Monforte, M. A.; Martín, A.; Menjón, B. The first structurally characterised homoleptic organovanadium(III) compound. *Chem. Commun.* **2001**, 2138–2139. (b) Alonso, P. J.; Forniés, J.; García-Monforte, M. A.; Martín, A.; Menjón, B. New Homoleptic Organometallic Derivatives of Vanadium(III) and Vanadium(IV): Synthesis, Characterization, and Study of Their Electrochemical Behaviour. *Chem.—Eur. J.* **2005**, *11*, 4713–4724. (c) Bucinsky, L.; Breza, M.; Malček, M.; Powers, D. C.; Hwang, S. J.; Krzystek, J.; Nocera, D. G.; Telsler, J. High-Frequency and -Field EPR (HFEP) Investigation of a Pseudotetrahedral Cr<sup>IV</sup> Siloxide Complex and Computational Studies of Related Cr<sup>IV</sup>L<sub>4</sub> Systems. *Inorg. Chem.* **2019**, *58*, 4907–4920.
- (27) Yang, L.; Powell, D. R.; Houser, R. P. Structural variation in copper(I) complexes with pyridylmethylamide ligands: structural analysis with a new four-coordinate geometry index,  $\tau_4$ . *Dalton Trans.* **2007**, 955–964.
- (28) Scott, M. J.; Wilisch, W. C. A.; Armstrong, W. H. Unprecedented example of four-coordination at a vanadium(II) center. Synthesis, structure, and properties of a reactive, nearly planar V(II) phenolate complex, [V(DIPP)<sub>4</sub>{Li(THF)}<sub>2</sub>] (DIPP = 2,6-diisopropylphenolate). *J. Am. Chem. Soc.* **1990**, *112*, 2429–2430.
- (29) Reinholdt, A.; Pividori, D.; Laughlin, A. L.; DiMucci, I. M.; MacMillan, S. N.; Jafari, M. G.; Gau, M. R.; Carroll, P. J.; Krzystek, J.; Ozarowski, A.; Telsler, J.; Lancaster, K. M.; Meyer, K.; Mindiola, D. J. A Mononuclear and High-Spin Tetrahedral Ti<sup>II</sup> Complex. *Inorg. Chem.* **2020**, *59*, 17834–17850.
- (30) Seok, W.-K.; Klapotke, T. M. Inorganic and Transition Metal Azides. *Bull. Korean Chem. Soc.* **2010**, *31*, 781–788.
- (31) Reinholdt, A.; Kwon, S.; Jafari, M. G.; Gau, M. R.; Carroll, P. J.; Lawrence, C.; Gu, J.; Baik, M.-H.; Mindiola, D. J. An Isolable Azide Adduct of Titanium(II) Follows Bifurcated Deazotation Pathways to an Imide. *J. Am. Chem. Soc.* **2022**, *144*, 527–537.
- (32) (a) Solan, G. A.; Cozzi, P. G.; Floriani, C.; Chiesi-Villa, A.; Rizzoli, C. Cyclodivanadazene Alkyl and Aryl Complexes. *Organometallics* **1994**, *13*, 2572–2574. (b) Odom, A. L.; Cummins, C. C. A Chromium(VI) Nitrido–Silylmethyl Complex and a Chromium(V)  $\mu$ -Nitrido Dimer: Synthetic and Structural Details. *Organometallics* **1996**, *15*, 898–900. (c) Zanolli-Gerosa, A.; Solari, E.; Giannini, L.; Floriani, C.; Chiesi-Villa, A.; Rizzoli, C. Stepwise Reduction of Dinitrogen to Nitride Assisted by Niobium Bonded to Oxygen Donor Atoms: The Potential of Reduced Forms of Niobium Calix[4]arene. *J. Am. Chem. Soc.* **1998**, *120*, 437–438. (d) Caselli, A.; Solari, E.; Scopelliti, R.; Floriani, C.; Re, N.; Rizzoli, C.; Chiesi-Villa, A. Dinitrogen Rearranging over a Metal–Oxo Surface and Cleaving to Nitride: From the End-On to the Side-On Bonding Mode, to the Stepwise Cleavage of the N≡N Bonds Assisted by Nb<sup>III</sup>-calix[4]arene. *J. Am. Chem. Soc.* **2000**, *122*, 3652–3670. (e) MacKay, B. A.; Patrick, B. O.; Fryzuk, M. D. Hydroalumination of a Dinuclear Tantalum Dinitrogen Complex: N–N Bond Cleavage and Ancillary Ligand Rearrangement. *Organometallics* **2005**, *24*, 3836–3841. (f) Akagi, F.; Matsuo, T.; Kawaguchi, H. Dinitrogen Cleavage by a Diniobium Tetrahydride Complex: Formation of a Nitride and Its Conversion into Imide Species. *Angew. Chem., Int. Ed.* **2007**, *46*, 8778–8781. (g) Tonzetich, Z. J.; Schrock, R. R.; Wampler, K. M.; Bailey, B. C.; Cummins, C. C.; Müller, P. A Tungsten(VI) Nitride Having a W<sub>2</sub>( $\mu$ -N)<sub>2</sub> Core. *Inorg. Chem.* **2008**, *47*, 1560–1567. (h) Keane, A. J.; Zavalij, P. Y.; Sita, L. R. N–N Bond Cleavage of Mid-Valent Ta(IV) Hydrazido and Hydrazidium Complexes Relevant to the Schrock Cycle for Dinitrogen Fixation. *J. Am. Chem. Soc.* **2013**, *135*, 9580–9583. (i) Akagi, F.; Suzuki, S.; Ishida, Y.; Hatanaka, T.; Matsuo, T.; Kawaguchi, H. Reactions of a Niobium Nitride Complex Prepared from Dinitrogen: Synthesis of Imide and Ureate Complexes and Ammonia Formation. *Eur. J. Inorg. Chem.* **2013**, *2013*, 3930–3936. (j) Keane, A. J.; Yonke, B. L.; Hirotsu, M.; Zavalij, P. Y.; Sita, L. R. Fine-Tuning the Energy Barrier for Metal-Mediated Dinitrogen N≡N Bond Cleavage. *J. Am. Chem. Soc.* **2014**, *136*, 9906–9909. (k) Camp, C.; Grant, L. N.; Bergman, R. G.; Arnold, J. Photoactivation of d<sup>0</sup> niobium imido azides: en route to nitrido complexes. *Chem. Commun.* **2016**, *52*, 5538–5541.

(33) Sun, W.; Holder, A.; Orvañanos, B.; Arca, E.; Zakutayev, A.; Lany, S.; Ceder, G. Thermodynamic Routes to Novel Metastable Nitrogen-Rich Nitrides. *Chem. Mater.* **2017**, *29*, 6936–6946.

(34) Robin, M. B.; Day, P. Mixed Valence Chemistry-A Survey and Classification. *Advances in Inorganic Chemistry and Radiochemistry*; Emelús, H. J., Sharpe, A. G., Eds.; Academic Press, 1968; Vol. 10, pp 247–422.

(35) Bencini, A.; Totti, F. On the importance of the biquadratic terms in exchange coupled systems: A post-HF investigation. *Inorg. Chim. Acta* **2008**, *361*, 4153–4156.

(36) Semenaka, V. V.; Nesterova, O. V.; Kokozay, V. N.; Dyakonenko, V. V.; Zubatyuk, R. I.; Shishkin, O. V.; Boča, R.; Jezierska, J.; Ozarowski, A. Cr<sup>III</sup>–Cr<sup>III</sup> Interactions in Two Alkoxo-Bridged Heterometallic Zn<sub>2</sub>Cr<sub>2</sub> Complexes Self-Assembled from Zinc Oxide, Reinecke's Salt, and Diethanolamine. *Inorg. Chem.* **2010**, *49*, 5460–5471.

(37) (a) Martini, G.; Ottaviani, M. F.; Seravalli, G. L. Electron spin resonance study of vanadyl complexes adsorbed on synthetic zeolites. *J. Phys. Chem.* **1975**, *79*, 1716–1720. (b) Atherton, N. M.; Shackleton, J. F. Proton ENDOR of VO(H<sub>2</sub>O)<sub>5</sub><sup>2+</sup> in (Mg(NH<sub>4</sub>)<sub>2</sub>(SO<sub>4</sub>)<sub>2</sub>·6H<sub>2</sub>O). *Mol. Phys.* **1980**, *39*, 1471–1485. (c) Pöppl, A.; Manikandan, P.; Köhler, K.; Maas, P.; Strauch, P.; Böttcher, R.; Goldfarb, D. Elucidation of Structure and Location of V(IV) Ions in Heteropolyacid Catalysts H<sub>4</sub>PVMo<sub>11</sub>O<sub>40</sub> as Studied by Hyperfine Sublevel Correlation Spectroscopy and Pulsed Electron Nuclear Double Resonance at W- and X-Band Frequencies. *J. Am. Chem. Soc.* **2001**, *123*, 4577–4584. (d) Baute, D.; Goldfarb, D. The <sup>17</sup>O Hyperfine Interaction in V<sup>17</sup>O(H<sub>2</sub><sup>17</sup>O)<sub>5</sub><sup>2+</sup> and Mn(H<sub>2</sub><sup>17</sup>O)<sub>6</sub><sup>2+</sup> Determined by High Field ENDOR Aided by DFT Calculations. *J. Phys. Chem. A* **2005**, *109*, 7865–7871.

(38) Mannikko, D.; Stoll, S. Vanadyl Porphyrin Speciation Based on Submegahertz Ligand Proton Hyperfine Couplings. *Energy Fuels* **2019**, *33*, 4237–4243.

(39) (a) Tran, B. L.; Washington, M. P.; Henckel, D. A.; Gao, X.; Park, H.; Pink, M.; Mindiola, D. J. A four coordinate parent imide via a titanium nitridyl. *Chem. Commun.* **2012**, *48*, 1529–1531. (b) Scheibel, M. G.; Askevold, B.; Heinemann, F. W.; Reijerse, E. J.; de Bruin, B.; Schneider, S. Closed-shell and open-shell square-planar iridium nitrido complexes. *Nat. Chem.* **2012**, *4*, 552–558. (c) Suarez, A. I. O.; Lyaskovskyy, V.; Reek, J. N. H.; van der Vlugt, J. I.; de Bruin, B. Complexes with Nitrogen-Centered Radical Ligands: Classification, Spectroscopic Features, Reactivity, and Catalytic Applications. *Angew. Chem., Int. Ed.* **2013**, *52*, 12510–12529. (d) Scheibel, M. G.; Wu, Y.; Stückl, A. C.; Krause, L.; Carl, E.; Stalke, D.; de Bruin, B.; Schneider, S. Synthesis and Reactivity of a Transient, Terminal Nitrido Complex of Rhodium. *J. Am. Chem. Soc.* **2013**, *135*, 17719–17722. (e) Scheibel, M. G.; Abbenseth, J.; Kinauer, M.; Heinemann, F. W.; Würtele, C.; de Bruin, B.; Schneider, S. Homolytic N–H Activation of Ammonia: Hydrogen Transfer of Parent Iridium Ammine, Amide, Imide, and Nitride Species. *Inorg. Chem.* **2015**, *54*, 9290–9302.

(40) (a) Bendix, J. [Cr(N)Cl<sub>4</sub>]<sup>2-</sup>: A Simple Nitrido Complex Synthesized by Nitrogen-Atom Transfer. *J. Am. Chem. Soc.* **2003**, *125*, 13348–13349. (b) Birk, T.; Bendix, J. Atom Transfer as a Preparative Tool in Coordination Chemistry. Synthesis and Characterization of Cr(V) Nitrido Complexes of Bidentate Ligands. *Inorg. Chem.* **2003**, *42*, 7608–7615. (c) Pittelkow, M.; Brock-Nannestad, T.; Bendix, J.; Christensen, J. B. Metalloporphyrin Dendrimers: Sensitive Corrole-Chromium(V)-Nitride Spin Probes for Studying the Solution Structure of Dendrimers. *Inorg. Chem.* **2011**, *50*, 5867–5869. (d) Hedegaard, E. D.; Schau-Magnussen, M.; Bendix, J. [Cr(N)(acac)<sub>2</sub>]: A simple chromium nitride complex and its reactivity towards late transition metals. *Inorg. Chem. Commun.* **2011**, *14*, 719–721. (e) Bendix, J.; Anthons, C.; Schau-Magnussen, M.; Brock-Nannestad, T.; Vibenholt, J.; Rehman, M.; Sauer, S. P. A. Heterobimetallic Nitride Complexes from Terminal Chromium(V) Nitride Complexes: Hyperfine Coupling Increases with Distance. *Angew. Chem., Int. Ed.* **2011**, *50*, 4480–4483.

(41) Meyer, K.; Bendix, J.; Bill, E.; Weyhermüller, T.; Wieghardt, K. Molecular and Electronic Structure of Nitridochromium(V) Complexes with Macrocyclic Amine Ligands. *Inorg. Chem.* **1998**, *37*, 5180–5188.

(42) (a) Mohan, M.; Holmes, S. M.; Butcher, R. J.; Jasinski, J. P.; Carrano, C. J. Synthesis, structure, and spectroscopic properties of vanadium(III) and -(IV) complexes containing hydridotris(pyrazolyl)-borate ligands. 3. *Inorg. Chem.* **1992**, *31*, 2029–2034. (b) Brunner, T. J.; Hascall, T.; Cowley, A. R.; Rees, L. H.; O'Hare, D. Variable Coordination Modes of Hydrotris(3-isopropyl-4-bromopyrazolyl)-borate (Tp') in Fe(II), Mn(II), Cr(II), and Cr(III) Complexes: Formation of MTp'Cl (M = Fe and Mn), Structural Isomerism in CrTp'<sub>2</sub>, and the Observation of Tp' - as an Uncoordinated Anion. *Inorg. Chem.* **2001**, *40*, 3170–3176.

## Recommended by ACS

### Controllable Electron Transfer in Mixed-Valence Bridged Norbornylogous Compounds: Ab Initio Calculation Combined with a Parametric Model and...

Shmuel Zilberg, Boris Tsukerblat, *et al.*

MAY 10, 2022  
THE JOURNAL OF PHYSICAL CHEMISTRY A

READ 

### Hydrides, Halides, and Polymers: Some Unexpected Intermediates on the Routes to First-Row Transition Metal M{N(SiMe<sub>3</sub>)<sub>2</sub>}<sub>n</sub> (n = 2, 3) Complexes

Cary R. Stennett and Philip P. Power

NOVEMBER 10, 2021  
INORGANIC CHEMISTRY

READ 

### Facile Transformations of a Binuclear Cp\*Co(II) Diamidonaphthalene Complex to Mixed-Valent Co(II)Co(III), Co(III)(μ-H)Co(III), and Co(III)(μ-OH)...

Yufang Xie, Wenguang Wang, *et al.*

JANUARY 20, 2022  
INORGANIC CHEMISTRY

READ 

### Synthesis, Characterization, and Reactivity of Low-Coordinate Titanium(III) Amido Complexes

Alejandro J. Cuellar De Lucio, T. Don Tilley, *et al.*

MAY 23, 2022  
ORGANOMETALLICS

READ 

Get More Suggestions >